

Supporting Information

Equilibrium Isotope Effects on Noncovalent Interactions in a Supramolecular Host-Guest System

Jeffrey S. Mugridge, Robert G. Bergman,* and Kenneth N. Raymond*

Department of Chemistry, University of California,
Berkeley, CA 94720-1460 and
Chemistry Division, Lawrence Berkeley National Laboratory,
Berkeley, CA, 94720, USA

Contact Information:

Prof. Robert G. Bergman, rbergman@berkeley.edu, Fax: (+1) 510-642-7714

Prof. Kenneth N. Raymond, raymond@socrates.berkeley.edu, Fax: (+1) 510-486-5283

Table of Contents

| | |
|--|-----------|
| Data for NMR titrations used to determine EIE on interior guest binding | S2 – S16 |
| Representative ¹ H NMR spectrum from unsuccessful interior EIE titrations | S17 |
| Representative ³¹ P{ ¹ H} NMR spectra from exterior EIE titrations | S18, S19 |
| Data for NMR titrations used to determine EIE on exterior guest binding | S20 – S29 |
| Error analysis used for exterior and interior EIE determination | S30 |
| Vibrational energy level population calculation | S31 – S32 |
| Atomic coordinates for DFT calculations | S33 – S38 |
| Details of M06-2X DFT calculations | S39 – S40 |
| Full citation for reference 47 | S40 |
| References | S41 |

Table S1. EIEs on interior binding of guest **2-d_n** to host **1** determined by linear regression using data from multiple $^{31}\text{P}\{^1\text{H}\}$ NMR titrations. The linear regressions with all of the NMR data used to determine the below values are shown in Figures S1 – S6. Raw concentration data and linear regressions for the individual NMR titrations are shown in Tables S2 – S6 and Figures S7 – S21. The values for Kd_0/Kd_2 and Kd_0/Kd_5 listed in Table 1 were obtained by dividing the directly measured values: $(Kd_0/Kd_9)/(Kd_2/Kd_9)$ and $(Kd_0/Kd_9)/(Kd_5/Kd_9)$, respectively. The errors for all values were obtained from the standard error on the slope of the linear regressions, fixed through zero.

| Ratio | EIE | Corresponding Figure |
|-------------|----------|----------------------|
| Kd_0/Kd_7 | 1.103(7) | S1 |
| Kd_0/Kd_9 | 1.14(1) | S2 |
| Kd_7/Kd_9 | 1.036(4) | S3 |
| Kd_5/Kd_9 | 1.14(2) | S4 |
| Kd_2/Kd_9 | 1.07(9) | S5 |
| Kd_2/Kd_5 | 0.94(1) | S6 |

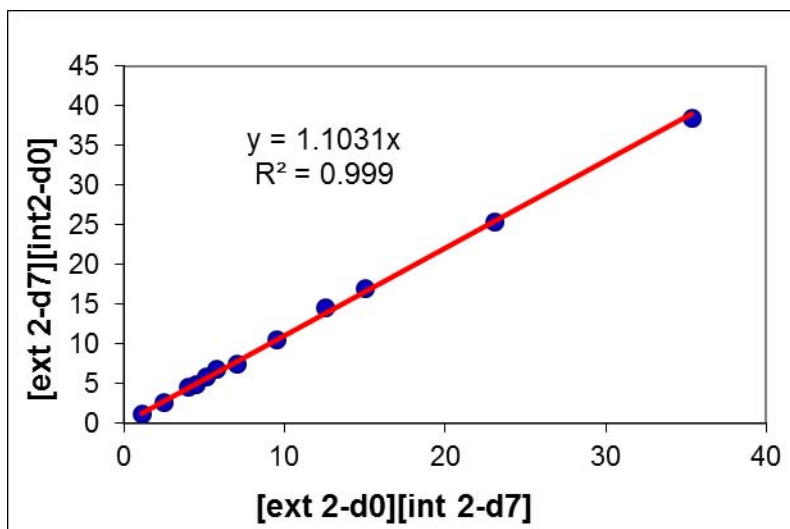


Figure S1. Linear regression to determine Kd_0/Kd_7 using all $^{31}\text{P}\{^1\text{H}\}$ NMR titration data.

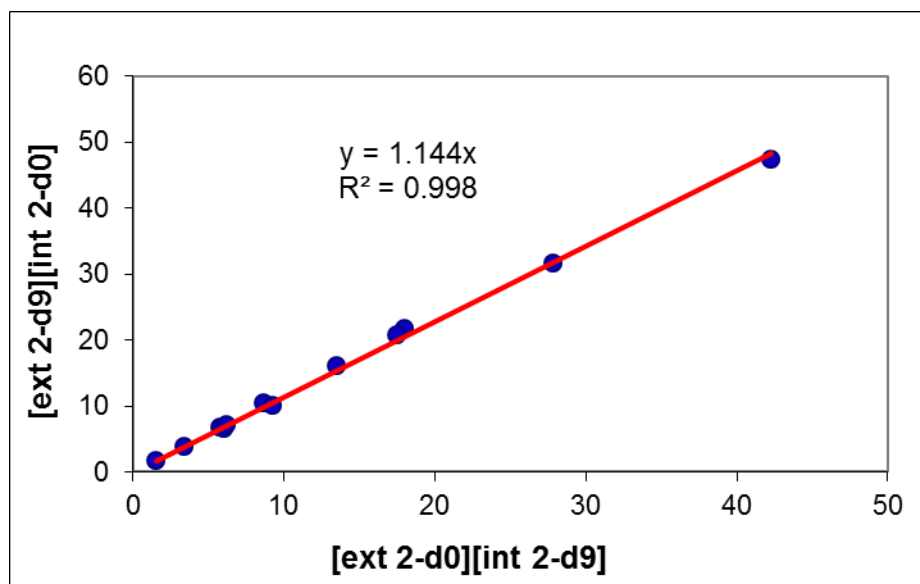


Figure S2. Linear regression to determine Kd_0/Kd_9 using all $^{31}\text{P}\{^1\text{H}\}$ NMR titration data.

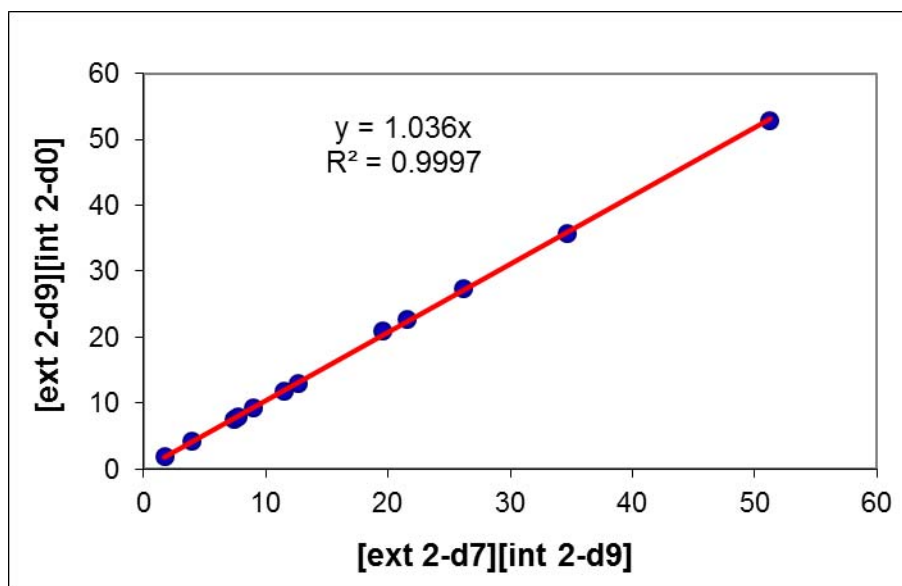


Figure S3. Linear regression to determine Kd_7/Kd_9 using all $^{31}\text{P}\{^1\text{H}\}$ NMR titration data.

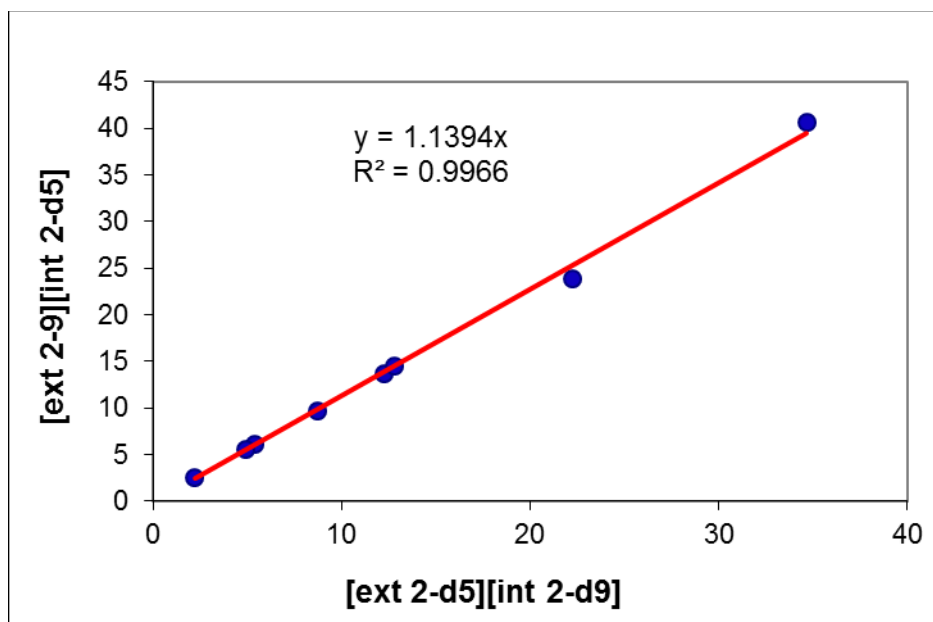


Figure S4. Linear regression to determine Kd_5/Kd_9 using all $^{31}\text{P}\{^1\text{H}\}$ NMR titration data.

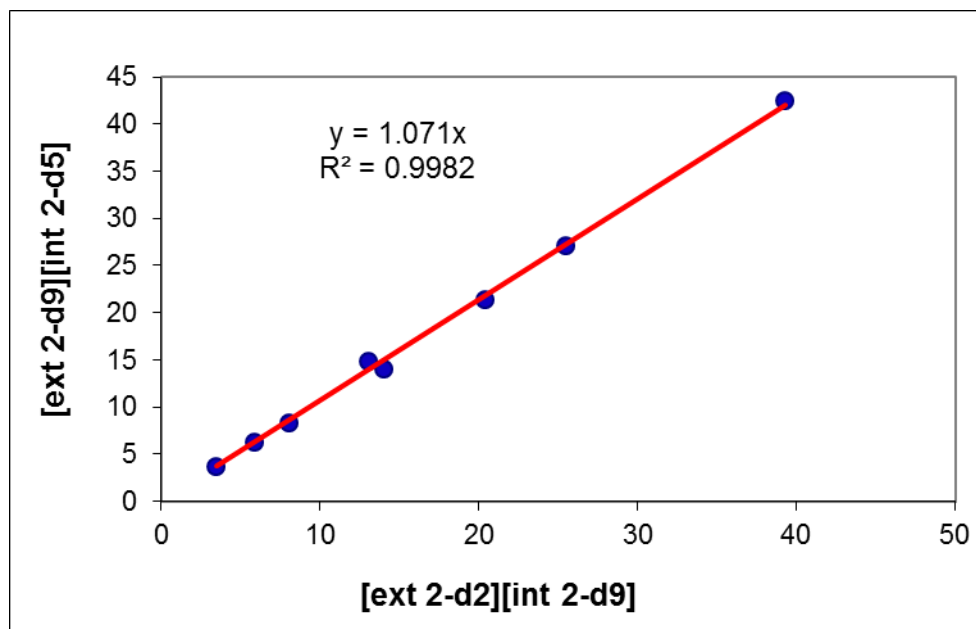


Figure S5. Linear regression to determine Kd_2/Kd_9 using all $^{31}\text{P}\{^1\text{H}\}$ NMR titration data.

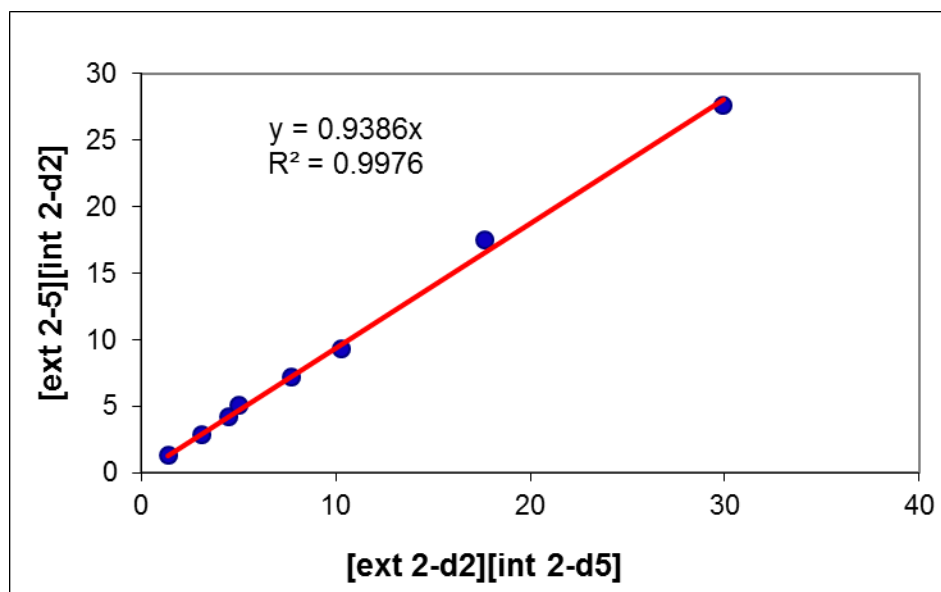


Figure S6. Linear regression to determine Kd_2/Kd_5 using all $^{31}\text{P}\{^1\text{H}\}$ NMR titration data.

Table S2. Raw concentration data and individual EIEs measured for each NMR tube (#1 - #4) in a single $^{31}\text{P}\{^1\text{H}\}$ NMR titration with $[\mathbf{1}] = 6 - 15$ mM; $[\mathbf{2-d}_n]/[\mathbf{1}] = 1.4$; $[\mathbf{2-d}_0] : [\mathbf{2-d}_7] : [\mathbf{2-d}_9] = 0.24 : 0.31 : 0.45$. These data correspond to the linear regressions shown in Figures S7 – S9.

| NMR Tube | [ext2- d_0] (mM) | [ext2- d_7] (mM) | [ext2- d_9] (mM) | [int2- d_0] (mM) | [int2- d_7] (mM) | [int2- d_9] (mM) | $\frac{Kd_0}{Kd_7}$ | $\frac{Kd_0}{Kd_9}$ | $\frac{Kd_7}{Kd_9}$ |
|----------|------------------------|------------------------|------------------------|------------------------|------------------------|------------------------|---------------------|---------------------|---------------------|
| #1 | 2.16 | 3.15 | 4.69 | 4.63 | 5.83 | 8.34 | 1.16 | 1.20 | 1.04 |
| #2 | 1.89 | 2.75 | 4.16 | 3.86 | 5.05 | 7.12 | 1.11 | 1.19 | 1.07 |
| #3 | 1.47 | 2.15 | 3.28 | 3.20 | 3.94 | 5.89 | 1.19 | 1.21 | 1.02 |
| #4 | 1.19 | 1.85 | 2.73 | 2.51 | 3.40 | 4.86 | 1.15 | 1.19 | 1.03 |

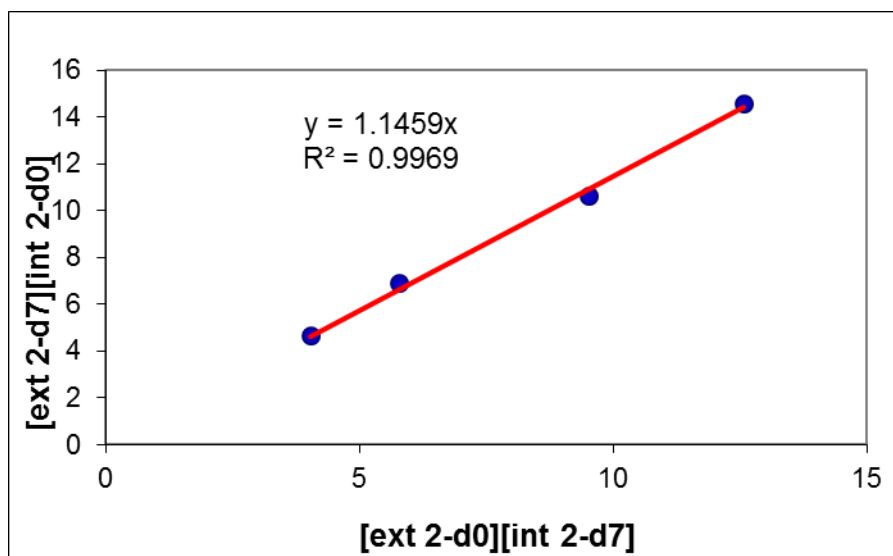


Figure S7. Linear regression to determine Kd_0/Kd_7 for guest **2-d_n** binding to the interior of host **1** for the single NMR titration described in Table S2 with $[2-d_n]/[1] = 1.4$.

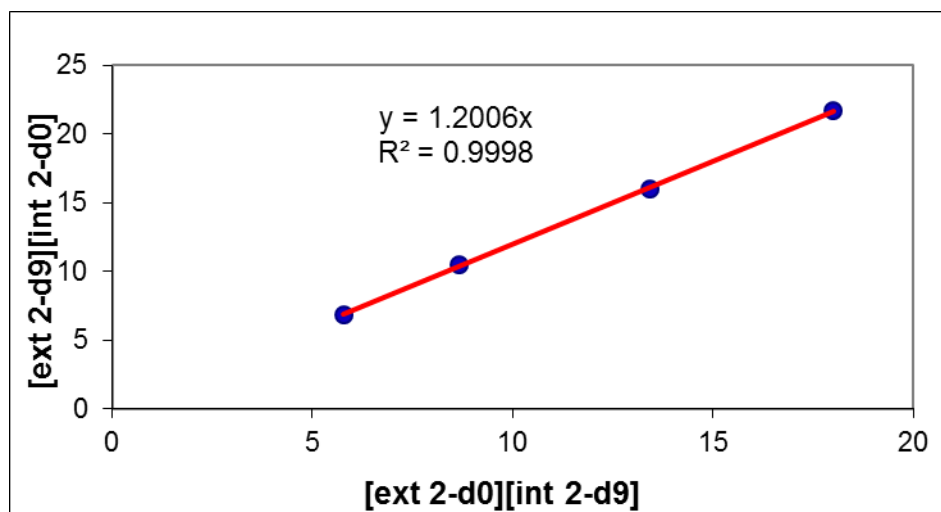


Figure S8. Linear regression to determine Kd_0/Kd_9 for guest **2-d_n** binding to the interior of host **1** for the single NMR titration described in Table S2 with $[2-d_n]/[1] = 1.4$.

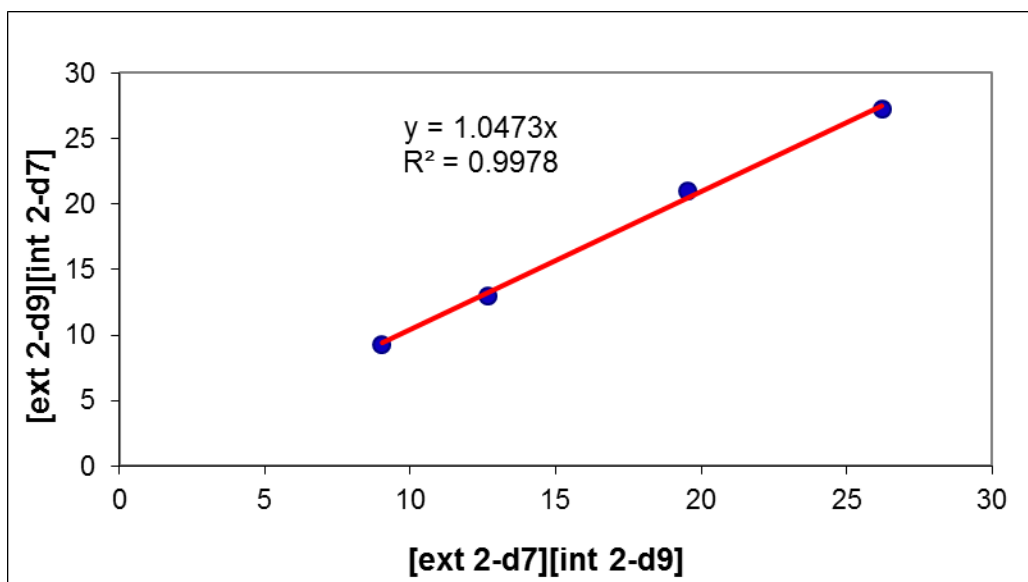


Figure S9. Linear regression to determine Kd_7/Kd_9 for guest **2-d_n** binding to the interior of host **1** for the single NMR titration described in Table S2 with $[2-d_n]/[1] = 1.4$.

Table S3. Raw concentration data and individual EIEs measured for each NMR tube (#1 - #4) in a single $^{31}\text{P}\{^1\text{H}\}$ NMR titration with $[1] = 6.3 - 15.8$ mM; $[2-d_n]/[1] = 2.1$; $[2-d_0] : [2-d_7] : [2-d_9] = 0.26 : 0.32 : 0.42$. These data correspond to the linear regressions shown in Figures S10 – S12.

| NMR Tube | [ext2-d ₀] (mM) | [ext2-d ₇] (mM) | [ext2-d ₉] (mM) | [int2-d ₀] (mM) | [int2-d ₇] (mM) | [int2-d ₉] (mM) | $\frac{Kd_0}{Kd_7}$ | $\frac{Kd_0}{Kd_9}$ | $\frac{Kd_7}{Kd_9}$ |
|----------|-----------------------------|-----------------------------|-----------------------------|-----------------------------|-----------------------------|-----------------------------|---------------------|---------------------|---------------------|
| #1 | 2.62 | 3.29 | 4.44 | 2.25 | 2.68 | 3.50 | 1.06 | 1.09 | 1.03 |
| #2 | 2.13 | 2.62 | 3.58 | 1.86 | 2.09 | 2.82 | 1.09 | 1.10 | 1.01 |
| #3 | 1.61 | 1.91 | 2.69 | 1.42 | 1.56 | 2.08 | 1.08 | 1.13 | 1.05 |
| #4 | 1.08 | 1.24 | 1.80 | 0.98 | 1.02 | 1.41 | 1.10 | 1.16 | 1.06 |

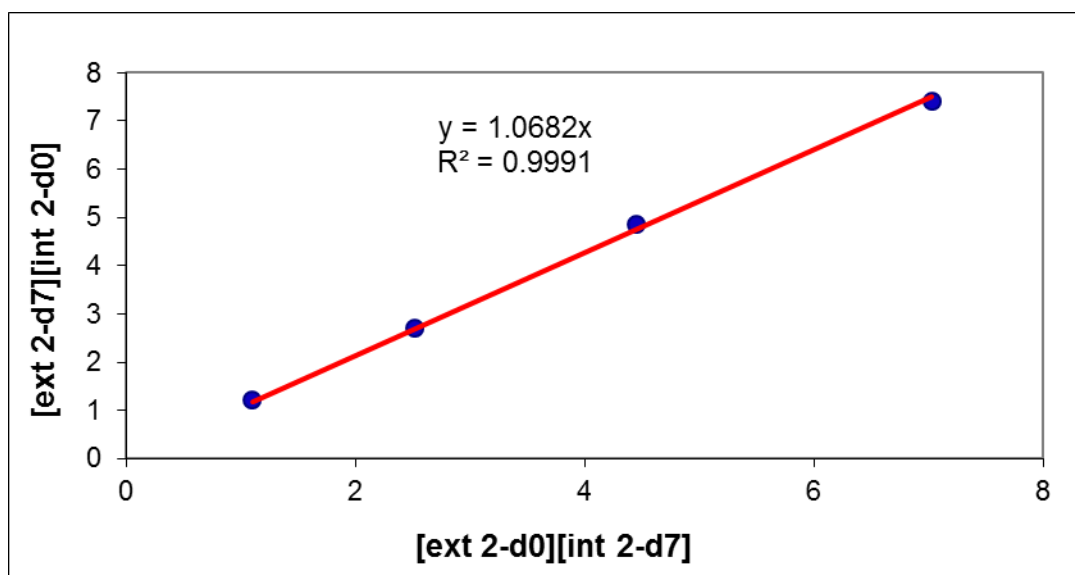


Figure S10. Linear regression to determine Kd_0/Kd_7 for guest **2-d_n** binding to the interior of host **1** for the single NMR titration described in Table S3 with $[2-d_n]/[1] = 2.1$.

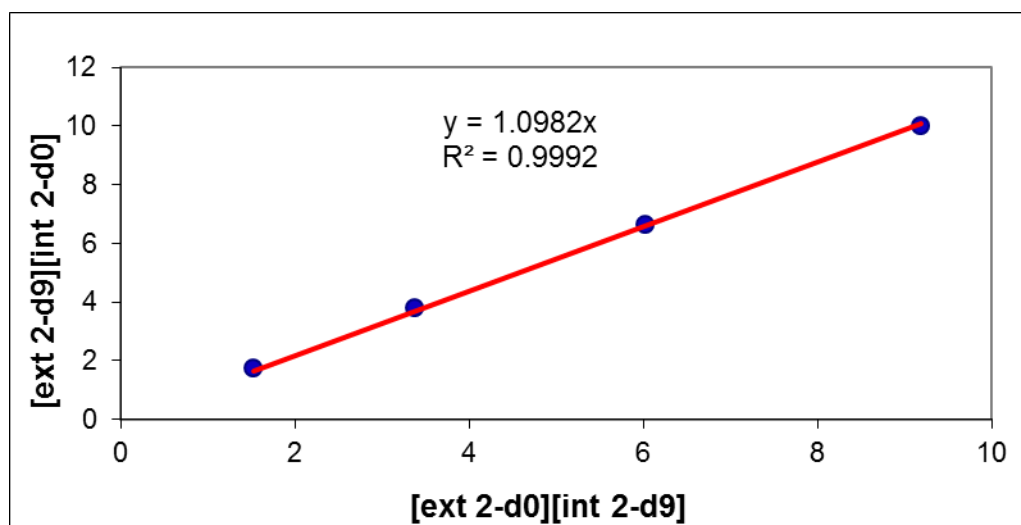


Figure S11. Linear regression to determine Kd_0/Kd_9 for guest **2-d_n** binding to the interior of host **1** for the single NMR titration described in Table S3 with $[2-d_n]/[1] = 2.1$.

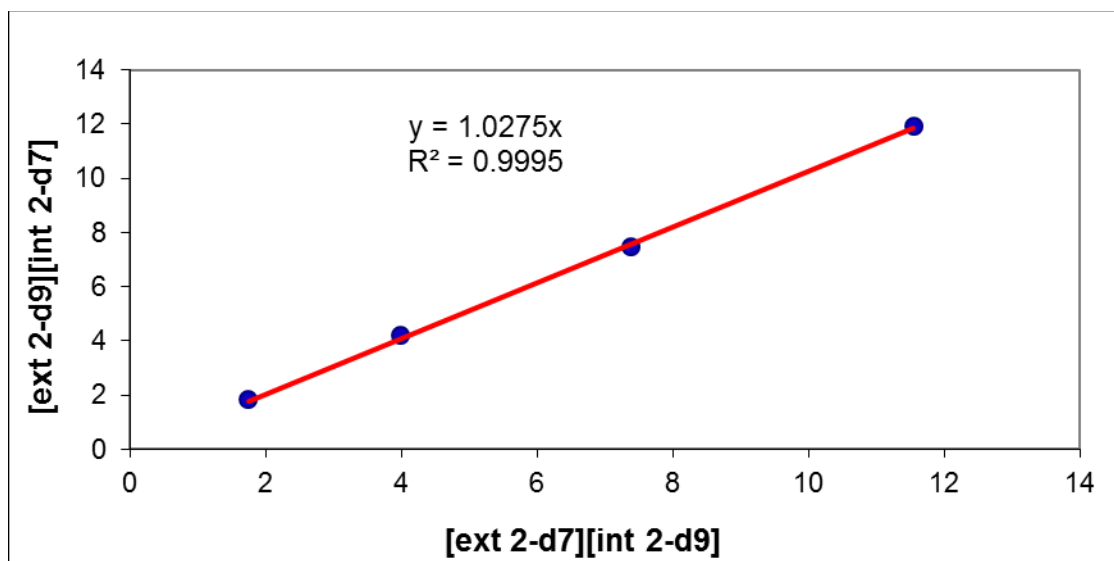


Figure S12. Linear regression to determine Kd_7/Kd_9 for guest **2-d_n** binding to the interior of host **1** for the single NMR titration described in Table S3 with $[2-d_n]/[1] = 2.1$.

Table S4. Raw concentration data and individual EIEs measured for each NMR tube (#1 - #4) in a single $^{31}\text{P}\{^1\text{H}\}$ NMR titration with $[1] = 5.6 - 13.9$ mM; $[2-d_n]/[1] = 3.2$; $[2-d_0] : [2-d_7] : [2-d_9] = 0.28 : 0.33 : 0.30$. These data correspond to the linear regressions shown in Figures S13 – S15.

| NMR Tube | [ext2-d ₀] (mM) | [ext2-d ₇] (mM) | [ext2-d ₉] (mM) | [int2-d ₀] (mM) | [int2-d ₇] (mM) | [int2-d ₉] (mM) | $\frac{Kd_0}{Kd_7}$ | $\frac{Kd_0}{Kd_9}$ | $\frac{Kd_7}{Kd_9}$ |
|----------|--------------------------------|--------------------------------|--------------------------------|--------------------------------|--------------------------------|--------------------------------|---------------------|---------------------|---------------------|
| #1 | 8.49 | 10.29 | 12.68 | 3.74 | 4.16 | 4.98 | 1.09 | 1.12 | 1.03 |
| #2 | 6.81 | 8.47 | 10.56 | 3.00 | 3.39 | 4.09 | 1.10 | 1.14 | 1.03 |
| #3 | 5.42 | 6.71 | 8.20 | 2.54 | 2.76 | 3.22 | 1.14 | 1.19 | 1.05 |
| #4 | 3.20 | 4.01 | 4.91 | 1.45 | 1.60 | 1.93 | 1.14 | 1.16 | 1.02 |

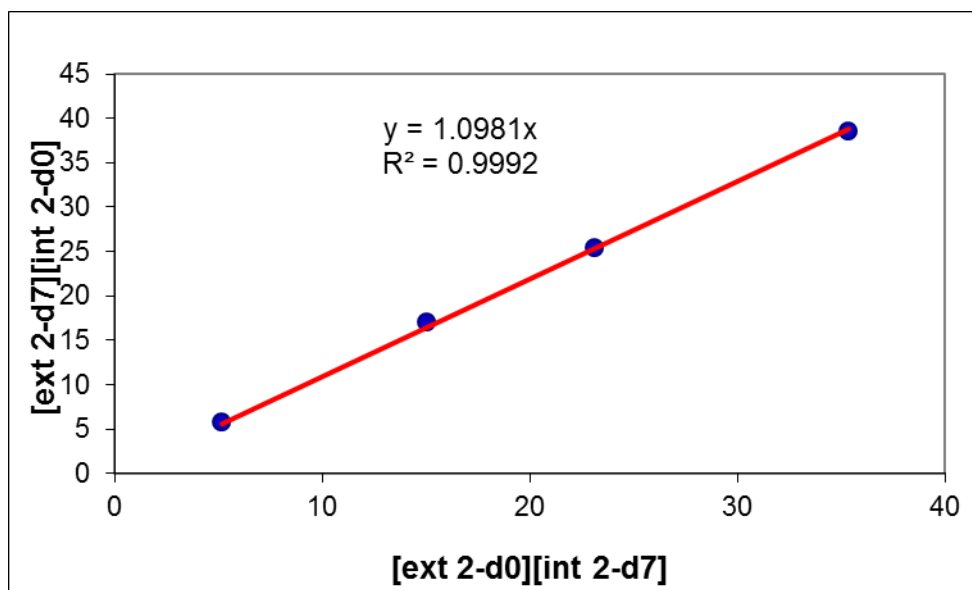


Figure S13. Linear regression to determine Kd_0/Kd_7 for guest **2-d_n** binding to the interior of host **1** for the single NMR titration described in Table S4 with $[2-d_n]/[1] = 3.2$.

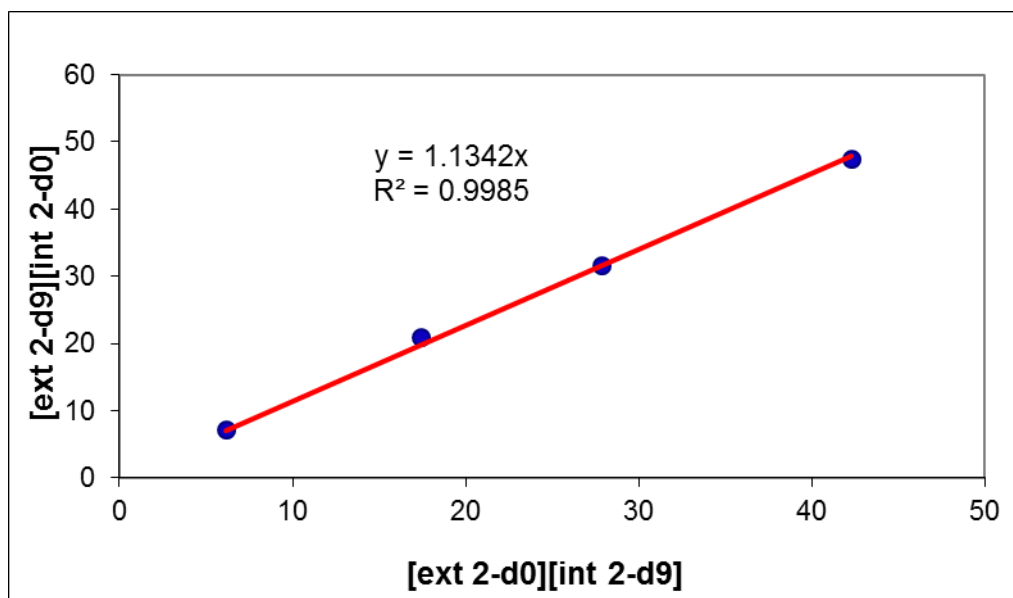


Figure S14. Linear regression to determine Kd_0/Kd_9 for guest **2-d_n** binding to the interior of host **1** for the single NMR titration described in Table S4 with $[2-d_n]/[1] = 3.2$.

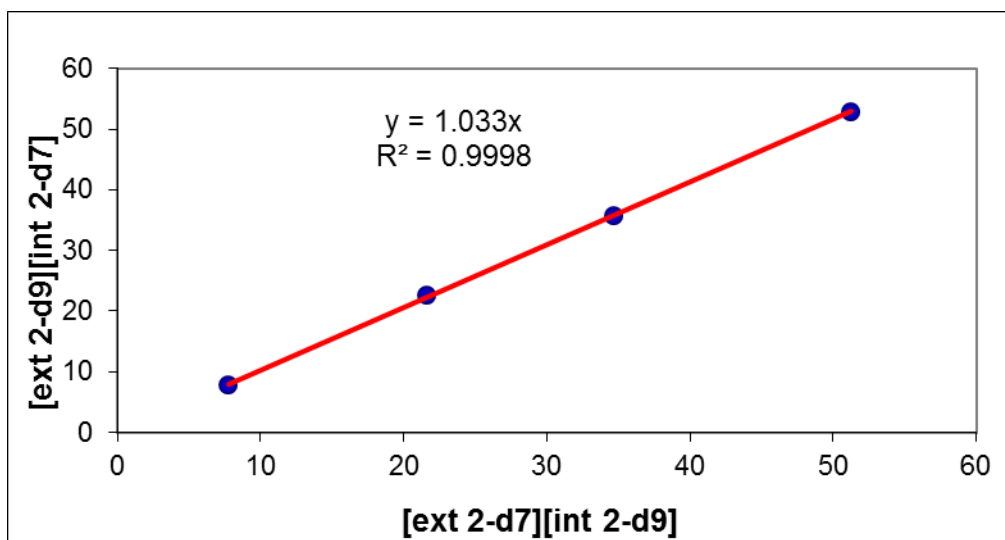


Figure S15. Linear regression to determine Kd_7/Kd_9 for guest **2-d_n** binding to the interior of host **1** for the single NMR titration described in Table S4 with $[2-d_n]/[1] = 3.2$.

Table S5. Raw concentration data and individual EIEs measured for each NMR tube (#1 - #4) in a single $^{31}\text{P}\{^1\text{H}\}$ NMR titration with $[1] = 6.7 - 16.8$ mM; $[2-d_n]/[1] = 1.5$; $[2-d_5] : [2-d_2] : [2-d_9] = 0.19 : 0.29 : 0.52$. These data correspond to the linear regressions shown in Figures S16 – S18.

| NMR Tube | [ext2-d ₀] (mM) | [ext2-d ₇] (mM) | [ext2-d ₉] (mM) | [int2-d ₀] (mM) | [int2-d ₇] (mM) | [int2-d ₉] (mM) | $\frac{Kd_5}{Kd_9}$ | $\frac{Kd_2}{Kd_9}$ | $\frac{Kd_2}{Kd_5}$ |
|----------|-----------------------------|-----------------------------|-----------------------------|-----------------------------|-----------------------------|-----------------------------|---------------------|---------------------|---------------------|
| #1 | 1.54 | 2.46 | 4.60 | 3.14 | 4.65 | 8.31 | 1.13 | 1.05 | 0.93 |
| #2 | 1.30 | 1.95 | 3.81 | 2.55 | 3.88 | 6.67 | 1.12 | 1.14 | 1.02 |
| #3 | 0.97 | 1.58 | 2.80 | 1.96 | 2.99 | 5.09 | 1.11 | 1.04 | 0.93 |
| #4 | 0.64 | 1.01 | 1.88 | 1.35 | 1.97 | 3.42 | 1.16 | 1.07 | 0.92 |

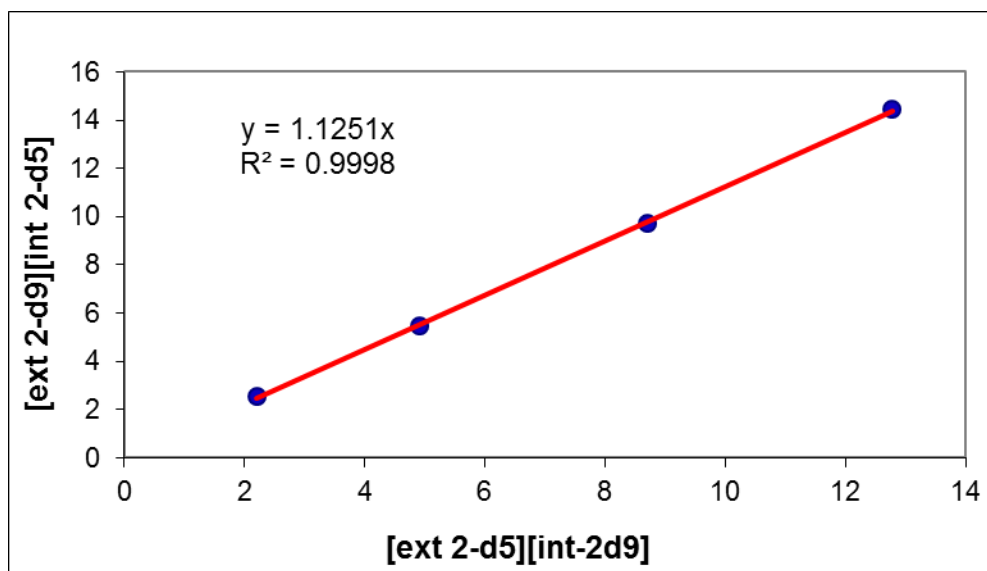


Figure S16. Linear regression to determine Kd_5/Kd_9 for guest $2-d_n$ binding to the interior of host **1** for the single NMR titration described in Table S5 with $[2-d_n]/[1] = 1.5$.

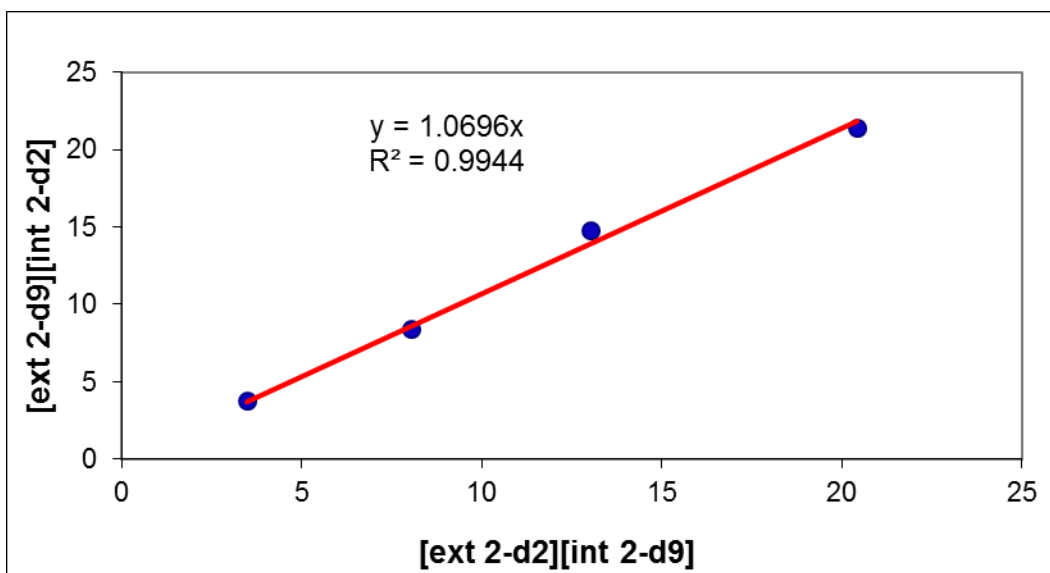


Figure S17. Linear regression to determine Kd_2/Kd_9 for guest $2-d_n$ binding to the interior of host **1** for the single NMR titration described in Table S5 with $[2-d_n]/[1] = 1.5$.

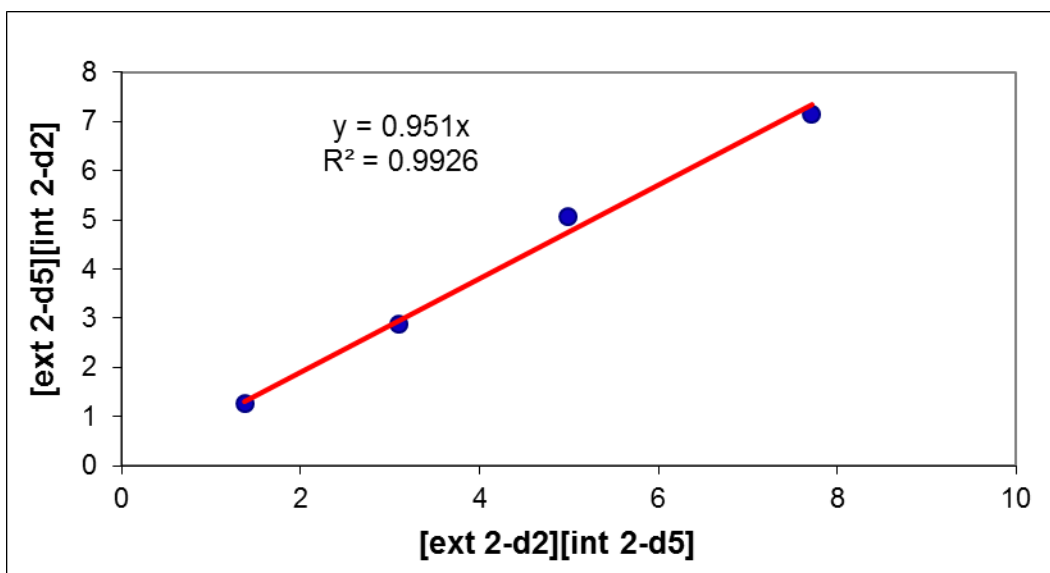


Figure S18. Linear regression to determine Kd_2/Kd_5 for guest $2-d_n$ binding to the interior of host **1** for the single NMR titration described in Table S5 with $[2-d_n]/[1] = 1.5$.

Table S6. Raw concentration data and individual EIEs measured for each NMR tube (#1 - #4) in a single $^{31}\text{P}\{^1\text{H}\}$ NMR titration with $[1] = 6.3 - 15.7$ mM; $[2-d_n]/[1] = 2.4$; $[2-d_5] : [2-d_2] : [2-d_9] = 0.28 : 0.31 : 0.41$. These data correspond to the linear regressions shown in Figures S19 – S21.

| NMR Tube | [ext2-d ₀] (mM) | [ext2-d ₇] (mM) | [ext2-d ₉] (mM) | [int2-d ₀] (mM) | [int2-d ₇] (mM) | [int2-d ₉] (mM) | $\frac{Kd_5}{Kd_9}$ | $\frac{Kd_2}{Kd_9}$ | $\frac{Kd_2}{Kd_5}$ |
|----------|-----------------------------|-----------------------------|-----------------------------|-----------------------------|-----------------------------|-----------------------------|---------------------|---------------------|---------------------|
| #1 | 6.03 | 6.83 | 9.29 | 4.38 | 4.58 | 5.75 | 1.17 | 1.08 | 0.92 |
| #2 | 4.83 | 5.52 | 7.47 | 3.20 | 3.63 | 4.61 | 1.07 | 1.06 | 0.99 |
| #3 | 3.66 | 4.18 | 5.54 | 2.46 | 2.54 | 3.35 | 1.11 | 1.01 | 0.91 |
| #4 | 2.55 | 2.77 | 3.79 | 1.62 | 1.65 | 2.12 | 1.13 | 1.06 | 0.94 |

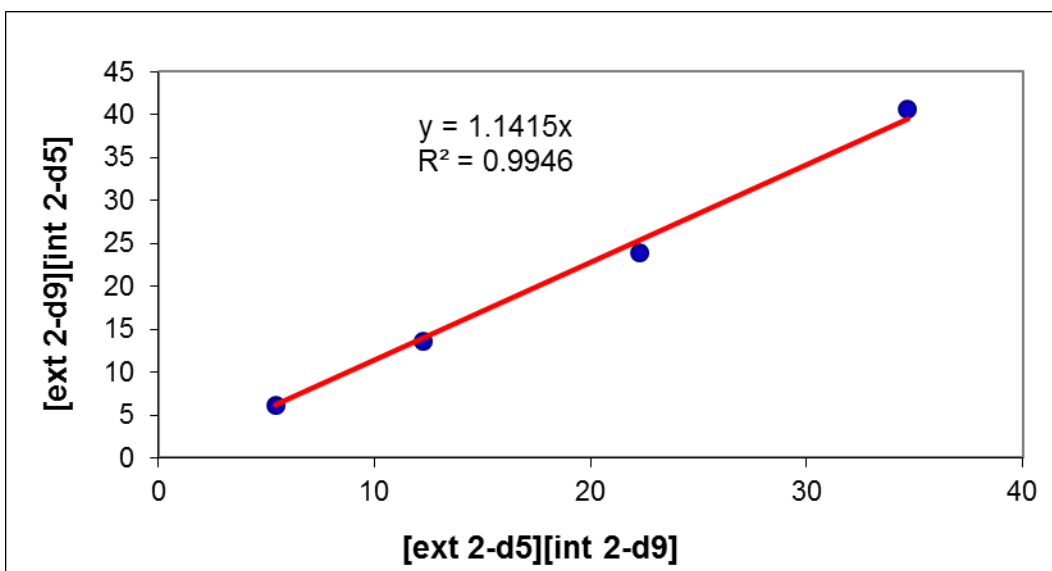


Figure S19. Linear regression to determine Kd_5/Kd_9 for guest **2-d_n** binding to the interior of host **1** for the single NMR titration described in Table S6 with $[2-d_n]/[1] = 2.4$.

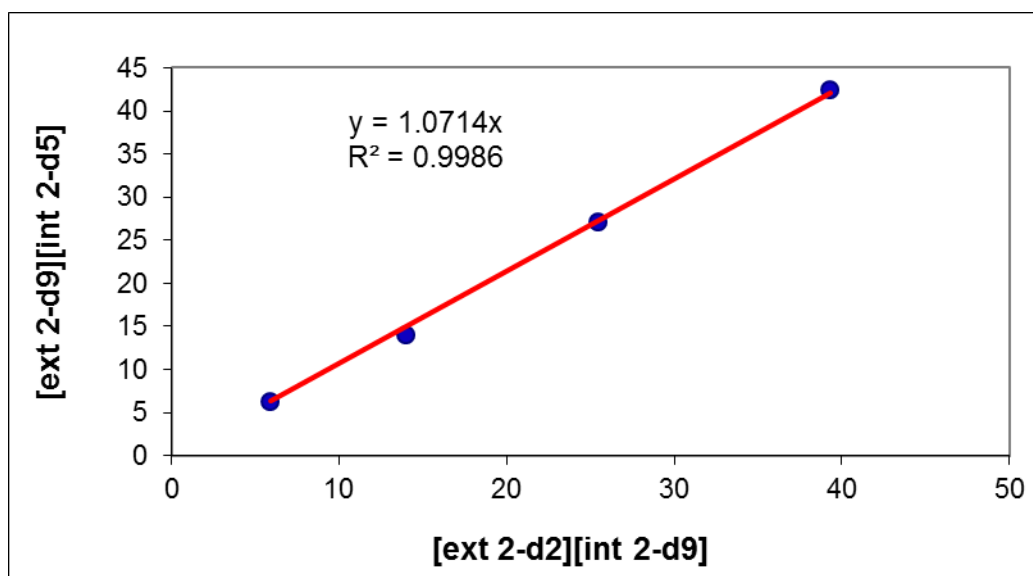


Figure S20. Linear regression to determine Kd_2/Kd_9 for guest **2-d_n** binding to the interior of host **1** for the single NMR titration described in Table S6 with $[2-d_n]/[1] = 2.4$.

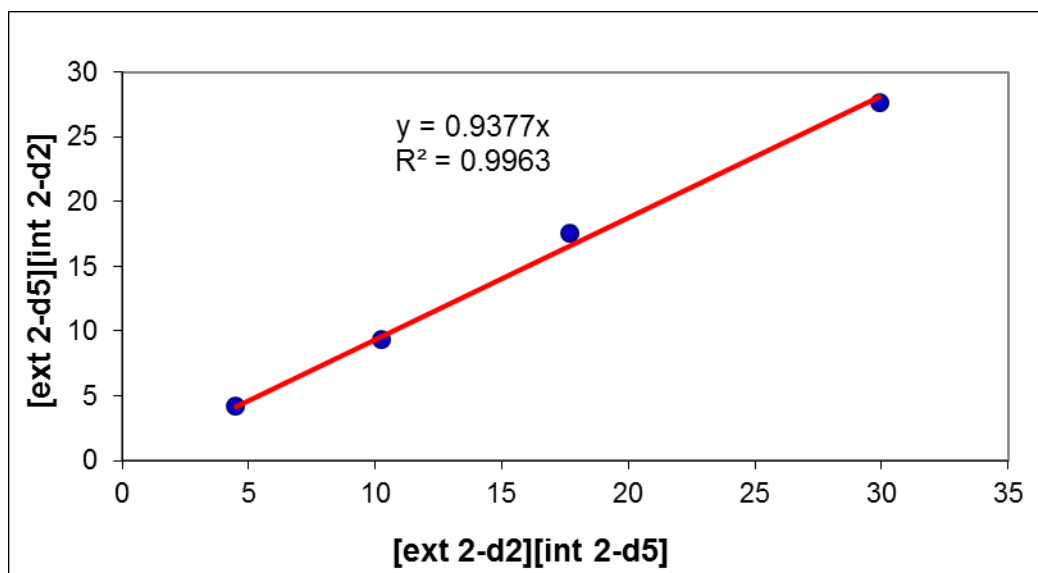


Figure S21. Linear regression to determine Kd_2/Kd_5 for guest $2-d_n$ binding to the interior of host **1** for the single NMR titration described in Table S6 with $[2-d_n]/[1] = 2.4$.

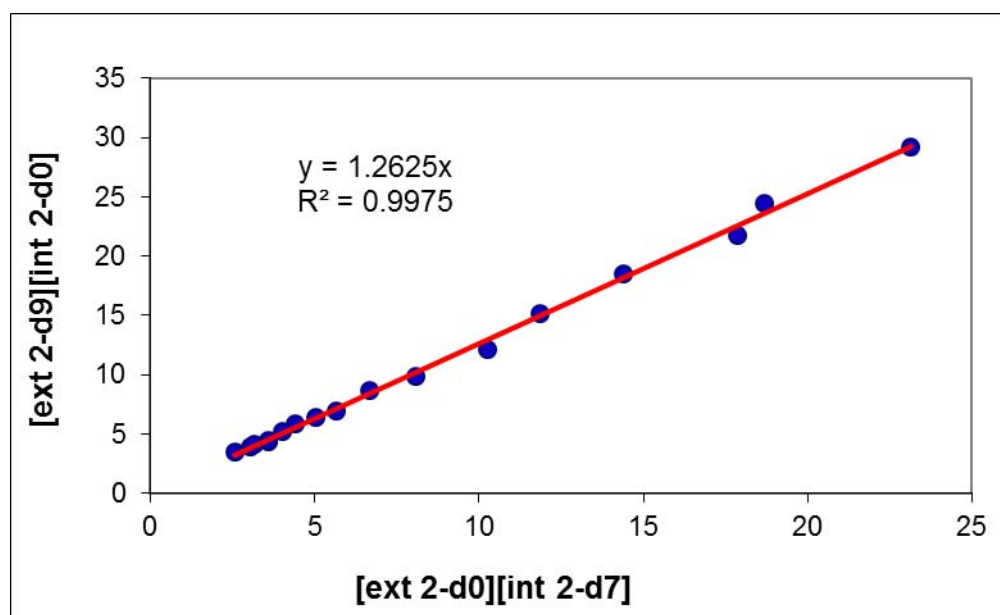


Figure S22. Plot of data from ^1H NMR titrations to determine the EIE on interior binding, competing $2-d_0$ versus $2-d_7$ in D_2O ($[1] = 7 - 17$ mM; $[2-d_n]/[1] = 1.3 - 1.4$; $[2-d_0]/[2-d_7] = 1.0 - 1.8$).

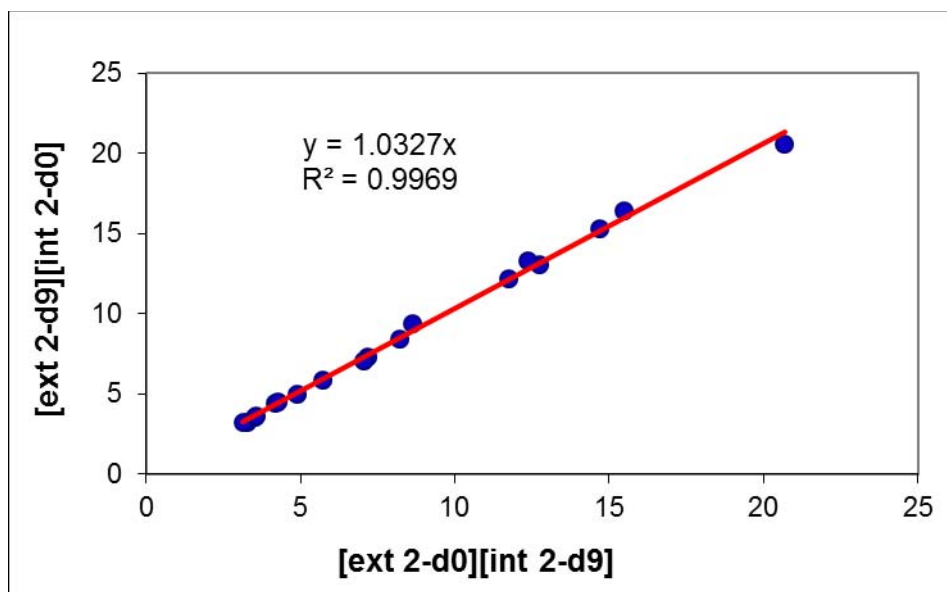


Figure S23. Plot of data from ^1H NMR titrations to determine the EIE on interior binding, competing $2\text{-}d_0$ versus $2\text{-}d_9$ in D_2O ($[\mathbf{1}] = 6 - 16$ mM; $[2\text{-}d_n]/[\mathbf{1}] = 1.2 - 1.4$; $[2\text{-}d_0]/[2\text{-}d_9] = 1.0 - 1.6$).

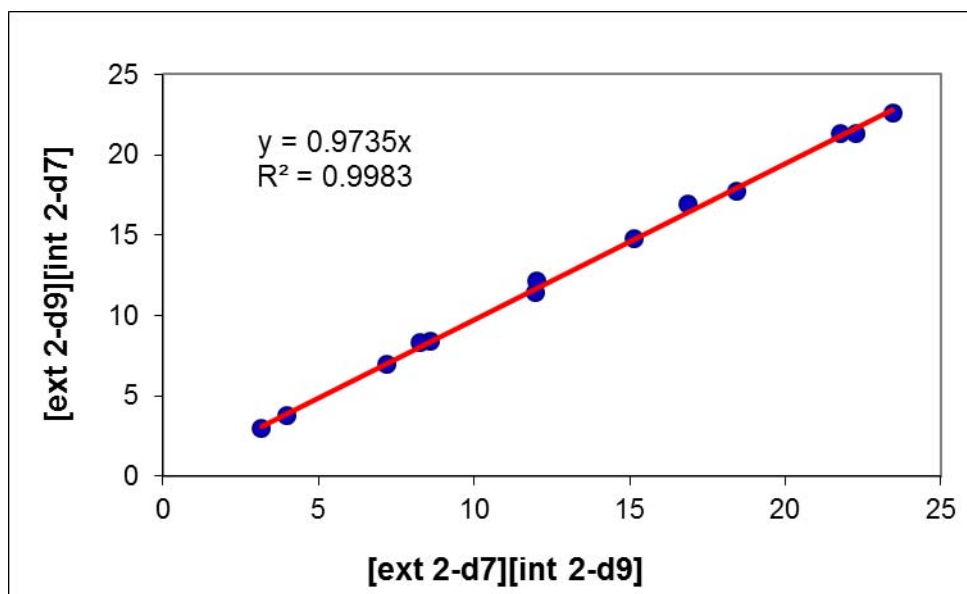


Figure S24. Plot of data from ^1H NMR titrations to determine the EIE on interior binding, competing $2\text{-}d_7$ versus $2\text{-}d_9$ in D_2O ($[\mathbf{1}] = 6 - 16$ mM; $[2\text{-}d_n]/[\mathbf{1}] = 1.4$; $[2\text{-}d_7]/[2\text{-}d_9] = 0.7 - 1.0$).

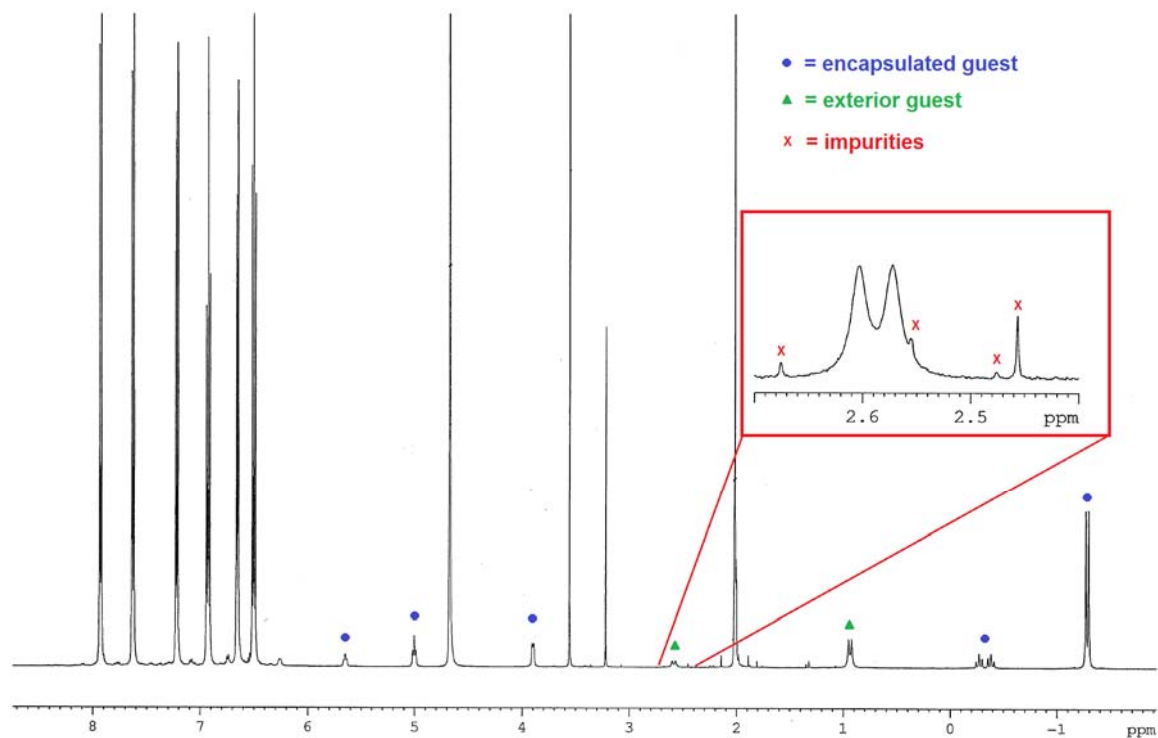


Figure S25. ^1H NMR spectrum from a titration competing $2\text{-}d_7$ with $2\text{-}d_9$ for interior binding. Small impurities overlap with the crucial exterior guest CH_2 resonance (boxed inset) at different points in the titration; relatively small changes in the exterior CH_2 integral lead to significant changes in the EIE, and this may be why the interior EIE values measured by ^1H NMR were not internally consistent. Blue circles denote encapsulated guest signals, green triangles denote unencapsulated guest signals and red x's denote impurities.

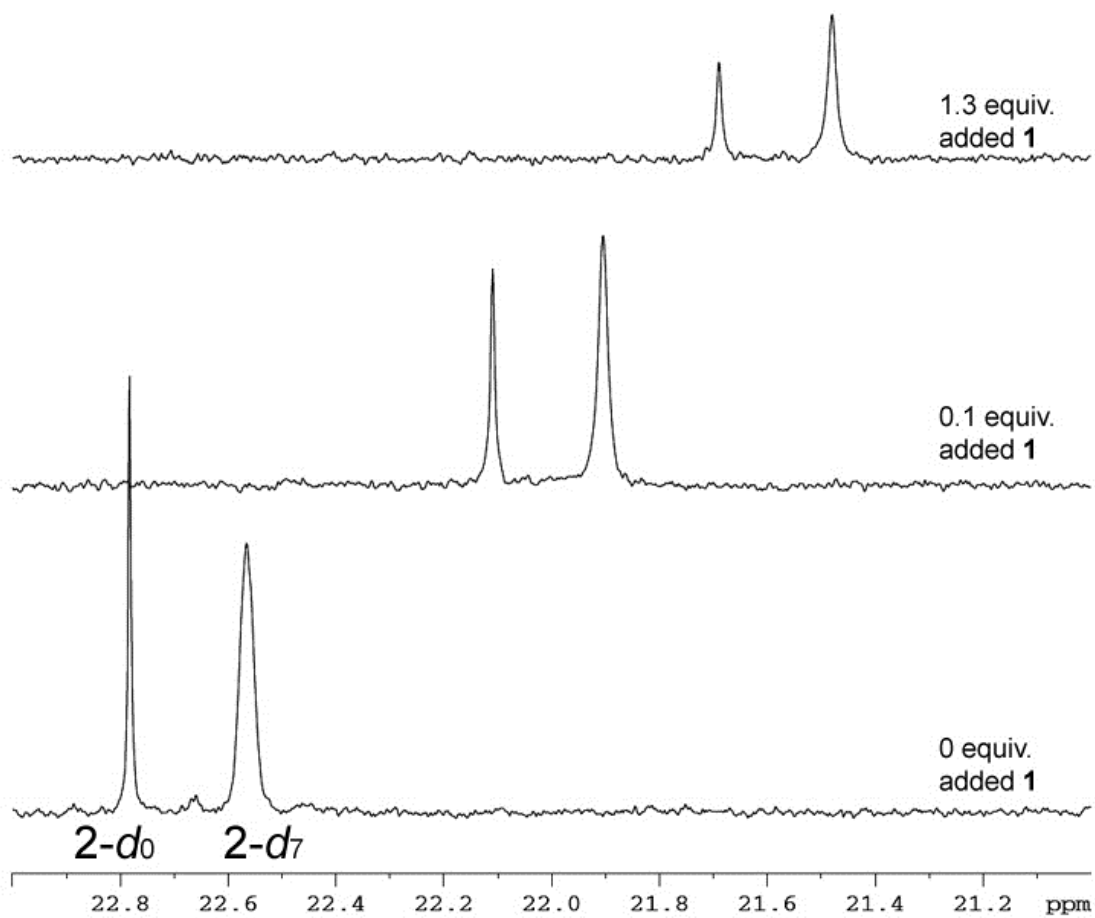


Figure S26. $^{31}\text{P}\{^1\text{H}\}$ NMR spectra for a typical **2-d₀** versus **2-d₇** titration at the beginning (bottom), middle and end (top) of the titration.

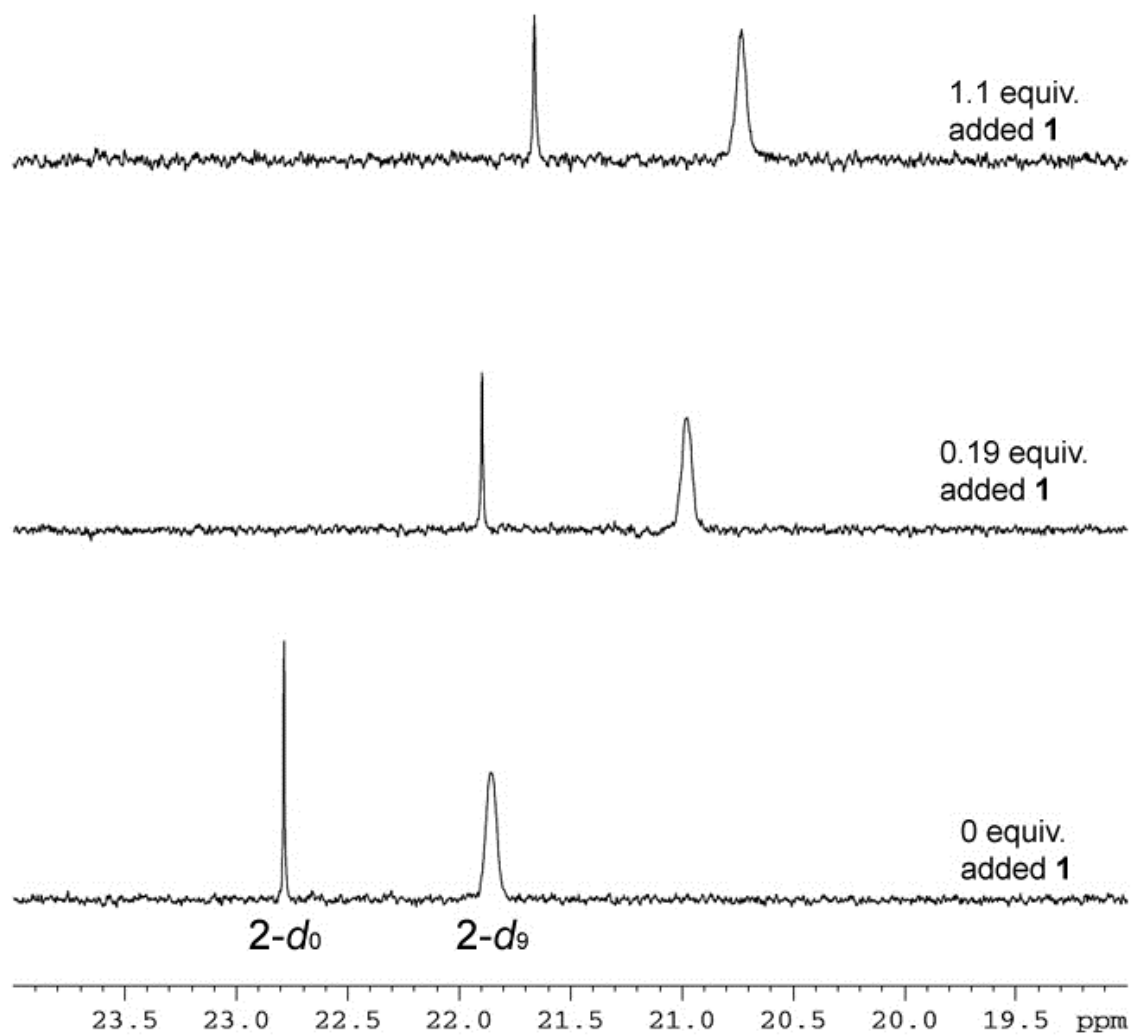


Figure S27. $^{31}\text{P}\{^1\text{H}\}$ NMR spectra for a typical $2\text{-}d_0$ versus $2\text{-}d_9$ titration at the beginning (bottom), middle and end (top) of the titration.

Table S7. Conditions and EIEs for individual titrations to determine the EIE on exterior binding of guest **2-d_n** to host **1**. The EIEs are independent of the concentration of isotopologues (total [**2-d_n**]), the ratio of the isotopologues (Ratio of **2-d_n**'s) or amount of the blocking guest NET_4^+ used (equiv. NET_4^+). The EIE values reported in Table 2 are weighted averages of the below titrations, according to Equation S1; errors on the EIE values were calculated according to Equations S2 – S4. Data for **2-d₀** versus **2-d₇** and **2-d₀** versus **2-d₉** are repeated from our earlier communication on the NMR titration method used to determine exterior EIEs.

| Isotopologues | Figure # for linear plot | total [2-d_n] (mM) | Ratio of 2-d_n 's ^a | Equiv. NET_4^+ (relative to 1) | EIE |
|---|--------------------------|---------------------------------------|---|---|--|
| 2-d₀ vs 2-d₇ | S28 | 34.8 | 1.0 : 2.3 | 2.1 | Kd₀/Kd₇ = 1.031(1) |
| | S29 | 27.9 | 1.0 : 2.4 | 5.0 | 1.0285(9) |
| | S30 | 43.8 | 1.0 : 2.3 | 4.3 | 1.0306(7) |
| | S31 | 25.9 | 1.0 : 3.5 | 4.6 | 1.0306(9) |
| 2-d₀ vs 2-d₉ | S32 | 26.1 | 1.0 : 2.0 | 2.5 | Kd₀/Kd₉ = 1.044(2) |
| | S33 | 24.8 | 1.0 : 2.1 | 5.3 | 1.053(5) |
| | S34 | 34.5 | 1.0 : 3.2 | 4.0 | 1.049(2) |
| 2-d₇ vs 2-d₉ | S35 | 22.0 | 1.0 : 0.8 | 5.3 | Kd₇/Kd₉ = 1.017(3) |
| 2-d₂ vs 2-d₅ vs 2-d₉ | S36, | 26.0 | 1.0 : 0.7 : 1.5 | 4.5 | Kd₂/Kd₉ = 1.035(2) |
| | S37 | | | | Kd₅/Kd₉ = 1.026(2) |

^a Ratio of **2-d_n**'s is the ratio of isotopologues in the NMR titration, listed in the same order as in the "Isotopologues" column of the table. For example, the ratio of **2-d_n**'s in the last entry is: [**2-d₂**] : [**2-d₅**] : [**2-d₉**] = 1.0 : 0.7 : 1.5.

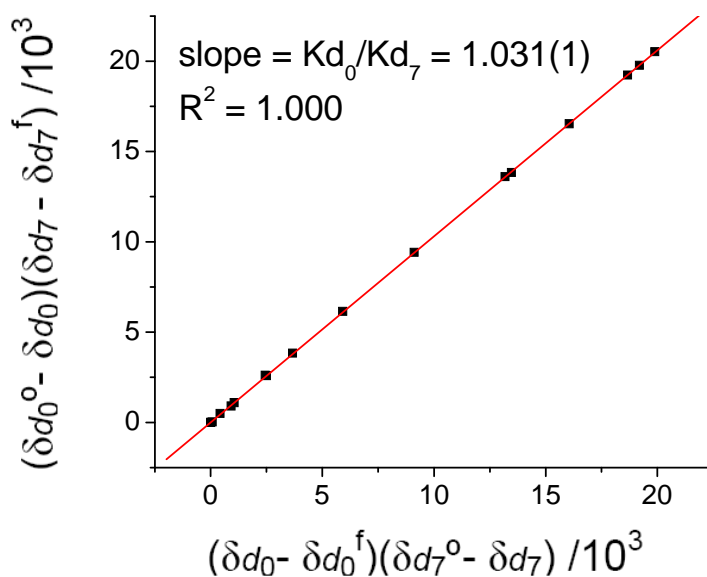


Figure S28. Linear plot to determine EIE on exterior binding of $2-d_n$ to host **1**. Data shown is from NMR titration competing $2-d_0$ vs $2-d_7$, with 2.1 equiv NEt_4^+ relative to **1**.

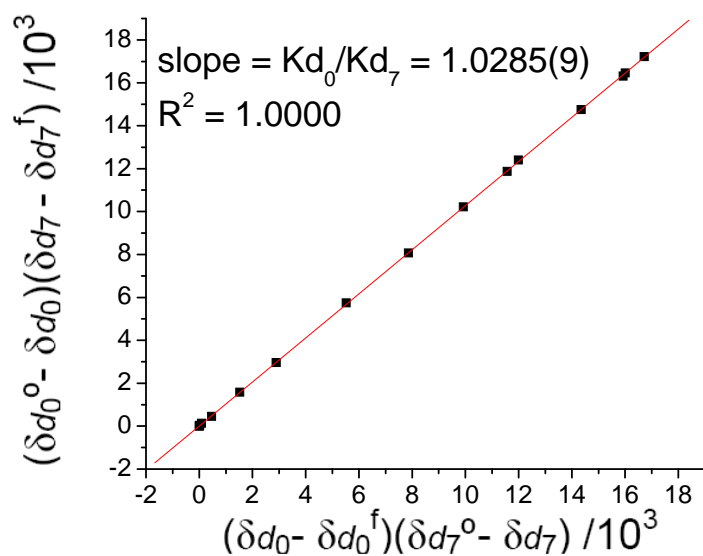


Figure S29. Linear plot to determine EIE on exterior binding of $2-d_n$ to host **1**. Data shown is from NMR titration competing $2-d_0$ vs $2-d_7$, with 5.0 equiv NEt_4^+ relative to **1**.

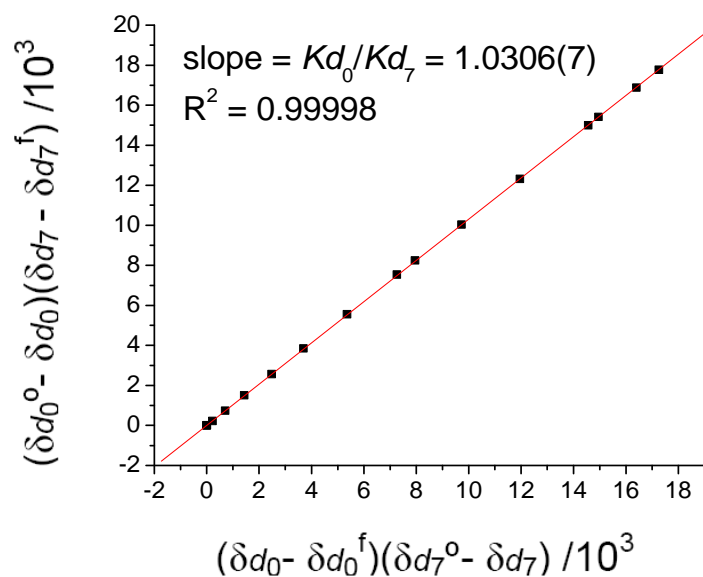


Figure S30. Linear plot to determine EIE on exterior binding of **2-d_n** to host **1**. Data shown is from NMR titration competing **2-d₀** vs **2-d₇**, with 4.3 equiv NEt₄⁺ relative to **1**.

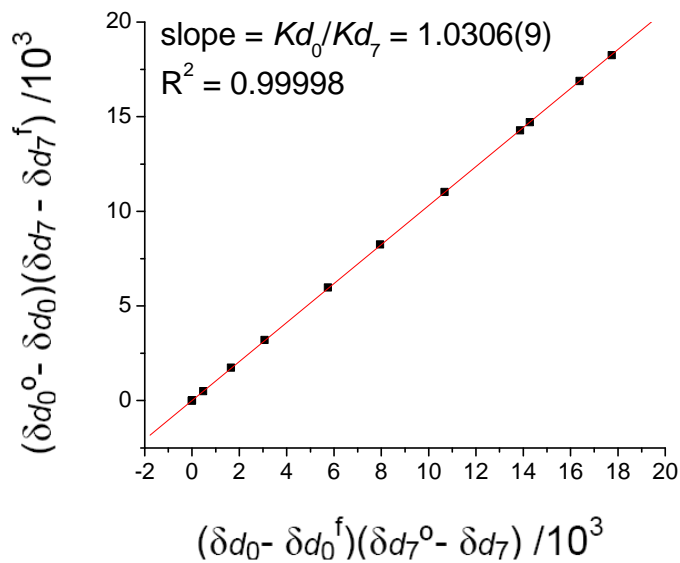


Figure S31. Linear plot to determine EIE on exterior binding of **2-d_n** to host **1**. Data shown is from NMR titration competing **2-d₀** vs **2-d₇**, with 4.6 equiv NEt₄⁺ relative to **1**.

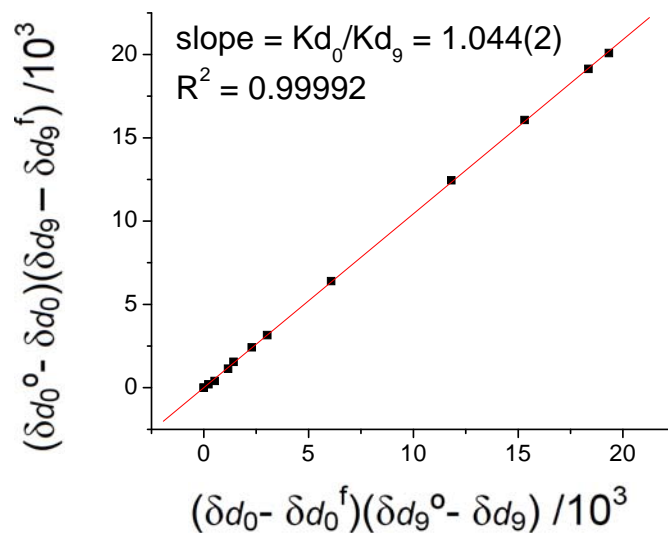


Figure S32. Linear plot to determine EIE on exterior binding of **2-d_n** to host **1**. Data shown is from NMR titration competing **2-d₀** vs **2-d₉**, with 2.5 equiv NEt₄⁺ relative to **1**.

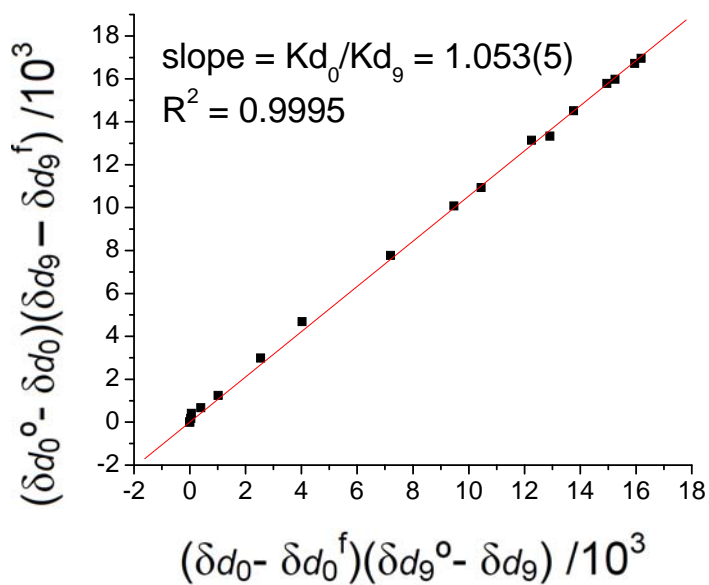


Figure S33. Linear plot to determine EIE on exterior binding of **2-d_n** to host **1**. Data shown is from NMR titration competing **2-d₀** vs **2-d₉**, with 5.3 equiv NEt₄⁺ relative to **1**.

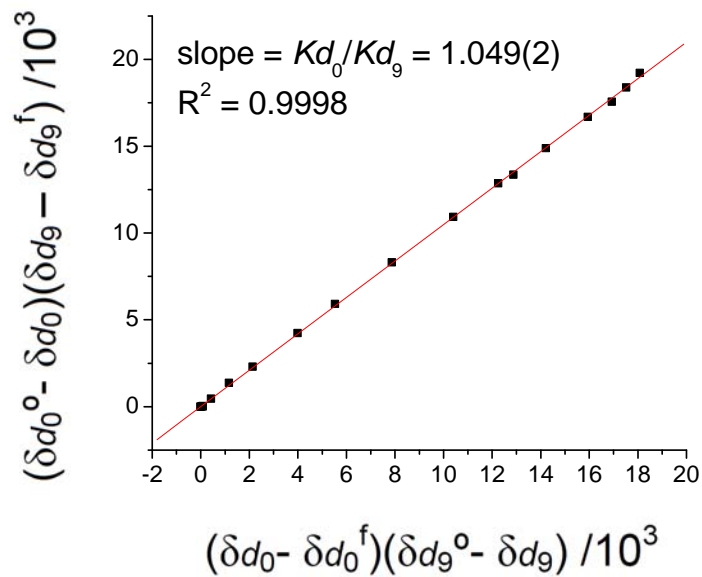


Figure S34. Linear plot to determine EIE on exterior binding of $2-d_n$ to host **1**. Data shown is from NMR titration competing $2-d_0$ vs $2-d_9$, with 4.0 equiv NEt_4^+ relative to **1**.

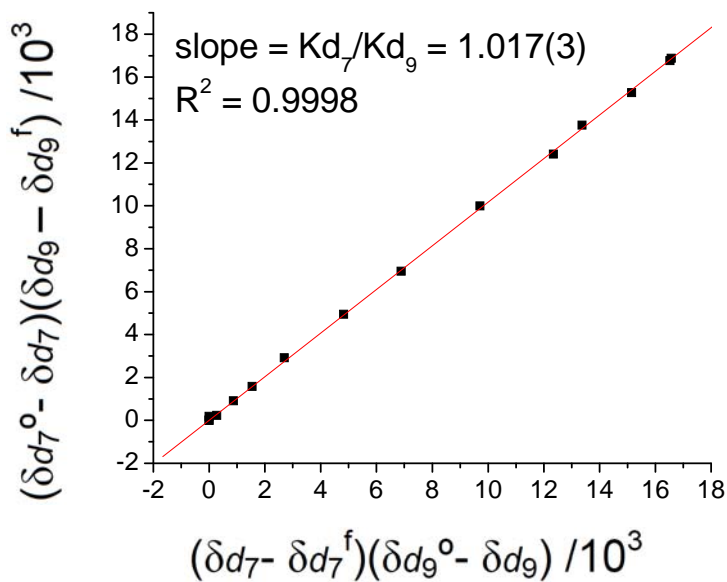


Figure S35. Linear plot to determine EIE on exterior binding of $2-d_n$ to host **1**. Data shown is from NMR titration competing $2-d_7$ vs $2-d_9$, with 5.3 equiv NEt_4^+ relative to **1**.

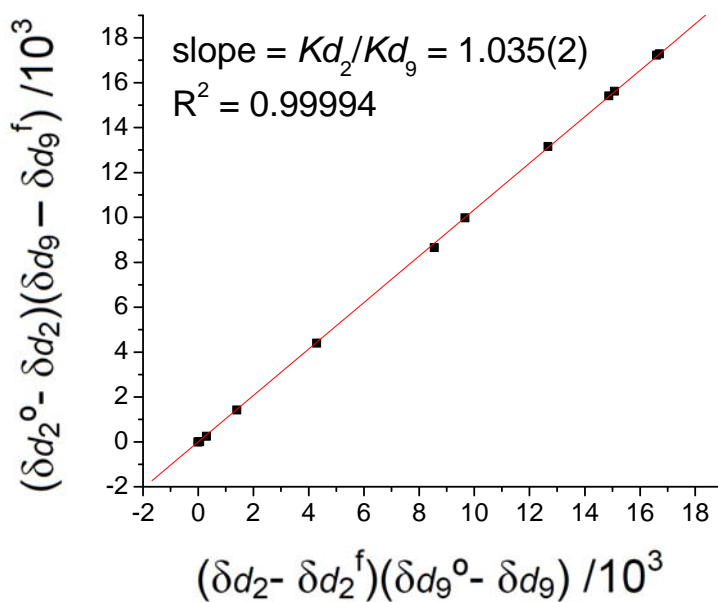


Figure S36. Linear plot to determine EIE on exterior binding of **2-d_n** to host **1**. Data shown is from NMR titration competing **2-d₂** vs **2-d₅** vs **2-d₉**, with 5 equiv NET_4^+ relative to **1**.

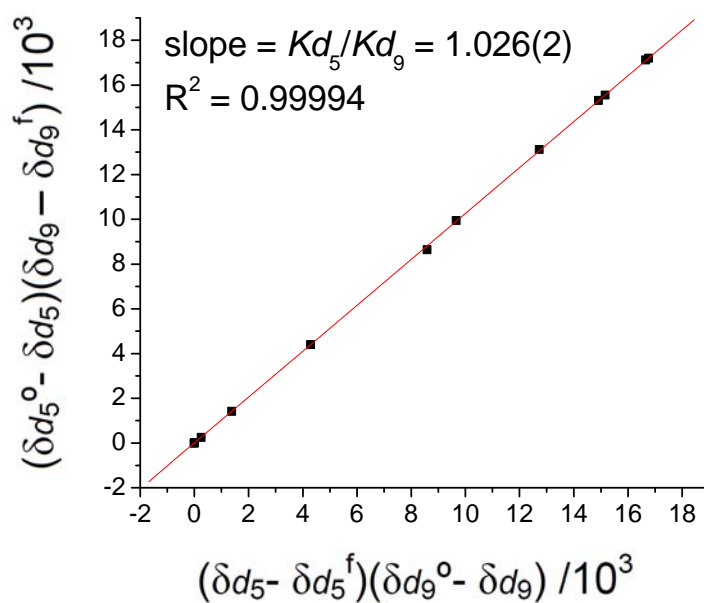


Figure S37. Linear plot to determine EIE on exterior binding of **2-d_n** to host **1**. Data shown is from NMR titration competing **2-d₂** vs **2-d₅** vs **2-d₉**, with 5 equiv NET_4^+ relative to **1**.

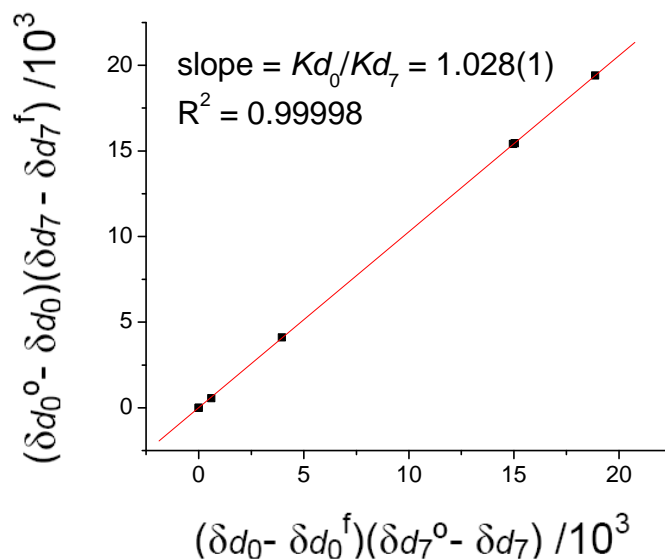


Figure S38. Linear plot from van't Hoff analysis of the EIE on exterior guest binding. Data shown is from NMR titration competing **2-d₀** vs **2-d₇** vs **2-d₉**, with 4 equiv NEt₄⁺ relative to **1**, at 300 K.

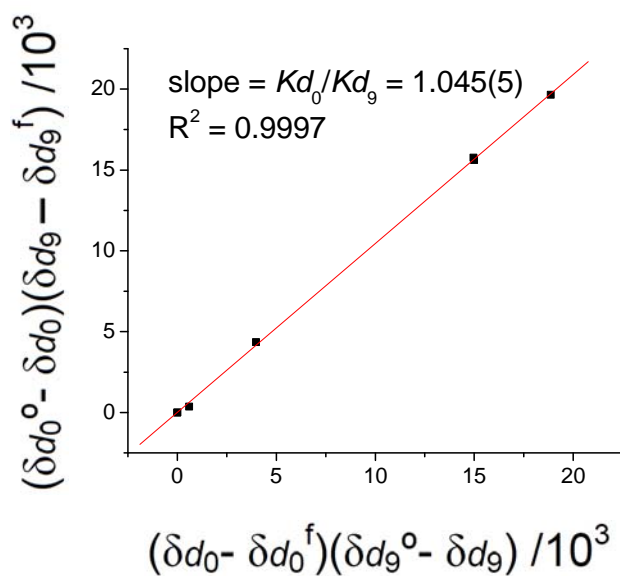


Figure S39. Linear plot from van't Hoff analysis of the EIE on exterior guest binding. Data shown is from NMR titration competing **2-d₀** vs **2-d₇** vs **2-d₉**, with 4 equiv NEt₄⁺ relative to **1**, at 300 K.

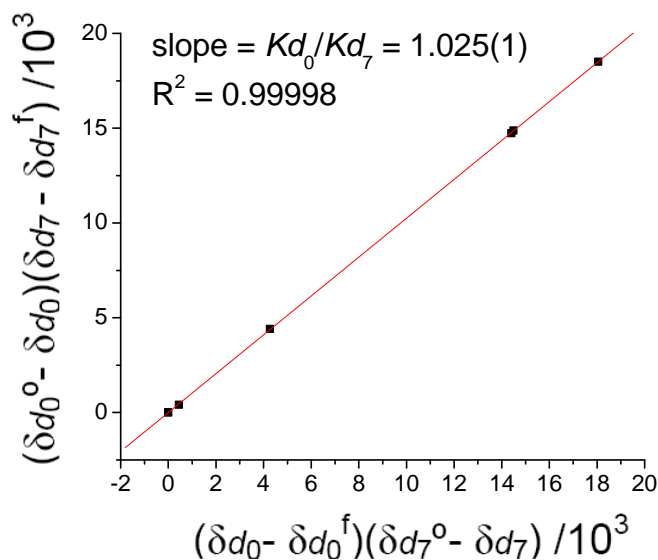


Figure S40. Linear plot from van't Hoff analysis of the EIE on exterior guest binding. Data shown is from NMR titration competing **2-d₀** vs **2-d₇** vs **2-d₉**, with 4 equiv NEt₄⁺ relative to **1**, at 307 K.

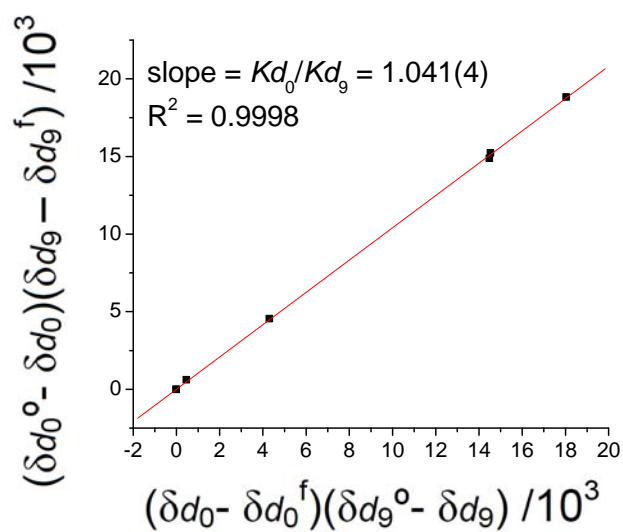


Figure S41. Linear plot from van't Hoff analysis of the EIE on exterior guest binding. Data shown is from NMR titration competing **2-d₀** vs **2-d₇** vs **2-d₉**, with 4 equiv NEt₄⁺ relative to **1**, at 307 K.

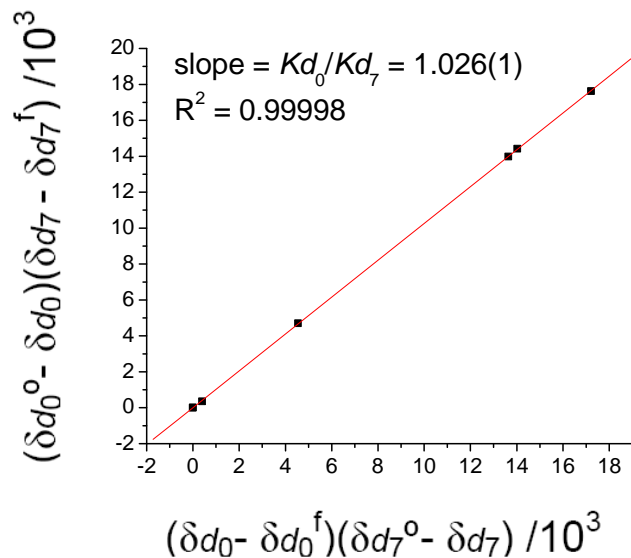


Figure S42. Linear plot from van't Hoff analysis of the EIE on exterior guest binding. Data shown is from NMR titration competing **2-d₀** vs **2-d₇** vs **2-d₉**, with 4 equiv NEt₄⁺ relative to **1**, at 314 K.

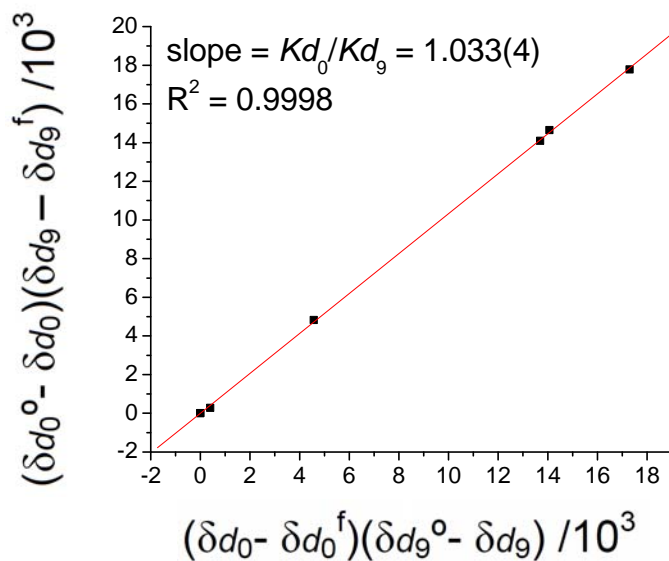


Figure S43. Linear plot from van't Hoff analysis of the EIE on exterior guest binding. Data shown is from NMR titration competing **2-d₀** vs **2-d₇** vs **2-d₉**, with 4 equiv NEt₄⁺ relative to **1**, at 314 K.

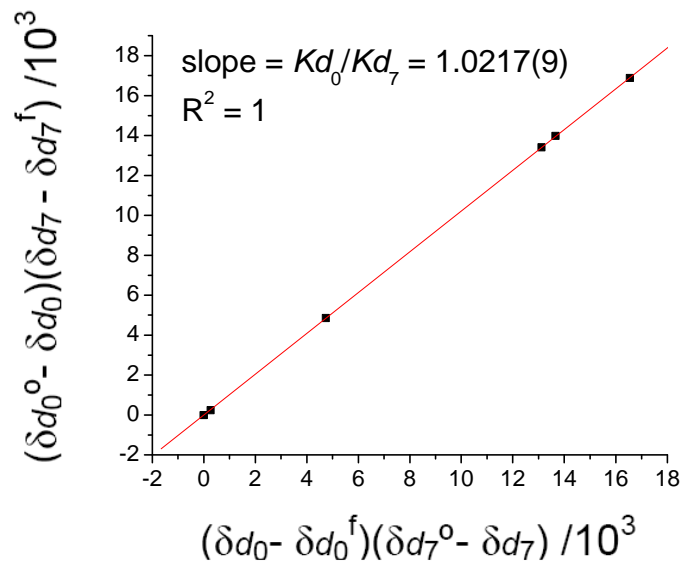


Figure S44. Linear plot from van't Hoff analysis of the EIE on exterior guest binding. Data shown is from NMR titration competing **2-d₀** vs **2-d₇** vs **2-d₉**, with 4 equiv NEt₄⁺ relative to **1**, at 320 K.

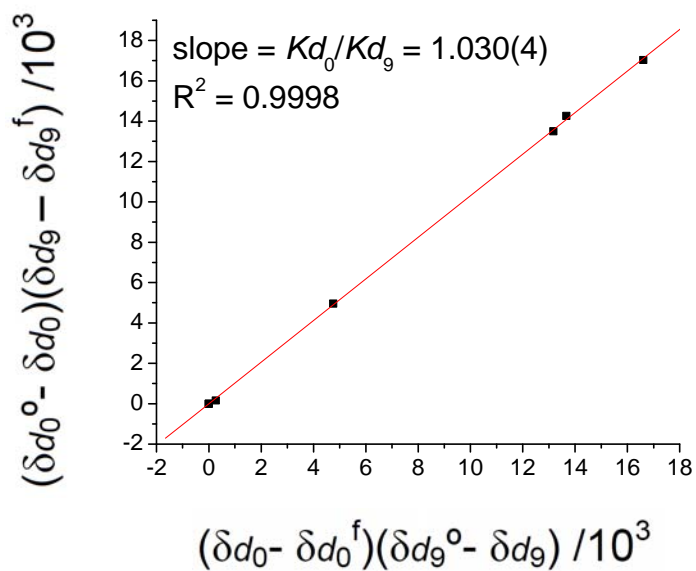


Figure S45. Linear plot from van't Hoff analysis of the EIE on exterior guest binding. Data shown is from NMR titration competing **2-d₀** vs **2-d₇** vs **2-d₉**, with 4 equiv NEt₄⁺ relative to **1**, at 320 K.

Error analysis for EIEs on interior and exterior binding:

For both interior and exterior binding, uncertainties in the measured EIEs were obtained directly from the error of the linear least-squares fit (constrained through zero) of the linearized NMR titration data (concentrations or chemical shifts, for interior and exterior, respectively) shown above.

The weighted average (\bar{x}) and uncertainty in the weighted average ($\sigma_{\bar{x}}$) for **2-d₀** vs **2-d₇** and **2-d₀** vs **2-d₉** exterior EIE titrations with different equiv NEt_4^+ were calculated using the following formulae:

Weighted average (\bar{x}):

$$\bar{x} = \frac{\sum_i \bar{x}_i / \sigma_i^2}{\sum_i 1 / \sigma_i^2} \quad \text{(Equation S1)}$$

x_i = data point

σ_i^2 = variance of x_i

Variance of \bar{x} :

$$\sigma_{\bar{x}}^2 = \left(\sum_i \frac{1}{\sigma_i^2} \right)^{-1} \quad \text{(Equation S2)}$$

The uncertainty in the EIE per deuterium value for both exterior and interior EIEs, $\sigma(\text{EIE}/D)$, was calculated using the following formula:

$$\sigma(\text{IE} / D) = \frac{\sigma(Kd_0 / Kd_n)}{n} \left(\frac{Kd_0}{Kd_n} \right)^{(1/n)-1} \quad \text{(Equation S3)}$$

Where n is the number of deuterium atoms, (Kd_0/Kd_n) is the measured IE and $\sigma(Kd_0/Kd_n)$ is the uncertainty in the measured EIE.

The uncertainty (σ) in EIE values that were calculated by multiplying or dividing directly measured EIE values ($\text{EIE}_1 * \text{EIE}_2$; where EIE_1 and EIE_2 are the measured values) is given by:

$$\sigma(\text{EIE}_1 * \text{EIE}_2) = (\text{EIE}_1 * \text{EIE}_2) \sqrt{\left(\frac{\sigma(\text{EIE}_1)}{\text{EIE}_1} \right)^2 + \left(\frac{\sigma(\text{EIE}_2)}{\text{EIE}_2} \right)^2} \quad \text{(Equation S4)}$$

Vibrational energy level population calculation to qualitatively address the entropic contribution to the EIE on exterior guest binding. To determine how changes in vibrational energy level populations affect the entropy of the host-guest association event, the differences in population for hypothetical, guest C–H and C–D wagging motions, in free solution versus bound to the host exterior, will be calculated. Wagging motions are chosen here because higher frequency vibrations, such as C–H/D stretching modes, have negligibly populated excited vibrational states: for a typical C–H stretch ($\sim 3000 \text{ cm}^{-1}$) at 298 K, only ~ 1 in 2,000,000 molecules exist in the first excited vibrational state. Ultimately, the initial vibrational motions chosen for this analysis are unimportant, since the qualitative trends in population changes will be the same regardless of the starting frequency.

First, consider a hypothetical C–H wag vibration with frequency, $\nu^{\text{CH}} = 1100 \text{ cm}^{-1} = 3.3 \times 10^{13} \text{ s}^{-1}$. Assuming a harmonic oscillator and using this C–H wag frequency in Equation S5, with the reduced mass of a C–H bond, $\mu^{\text{CH}} = 0.92$, the vibrational force constant, k , for the C–H wagging mode is calculated at 66 N/m. Since isotopic substitution leaves the force constant unchanged, an equivalent C–D bond ($\mu^{\text{CD}} = 1.71$) will have a wagging frequency of $\nu^{\text{CD}} = 2.42 \times 10^{13} \text{ s}^{-1}$. The energy of a vibrational energy level ($E_{v=n}$) is given by Equation S6, where h is Planck's constant. The energies of the first two vibrational energy levels ($v=0$, $v=1$) for the C–H and C–D wagging motions are then calculated as: $E_{v=0}^{\text{CH}} = 1.57 \text{ kcal/mol}$, $E_{v=1}^{\text{CH}} = 4.72 \text{ kcal/mol}$, $E_{v=0}^{\text{CD}} = 1.16 \text{ kcal/mol}$, and $E_{v=1}^{\text{CD}} = 3.47 \text{ kcal/mol}$. The energy differences between the vibrational energy levels are: $\Delta E^{\text{CH}} = 3.15 \text{ kcal/mol}$ and $\Delta E^{\text{CD}} = 2.31 \text{ kcal/mol}$.

$$\nu = \frac{1}{2\pi} \sqrt{\frac{k}{\mu}} \quad (\text{Equation S5})$$

Where k is the force constant and the reduced mass, $\mu = m_1 m_2 / (m_1 + m_2)$, where m_1 and m_2 are the masses.

$$E_{v=n} = \left(\frac{1}{2} + n \right) h\nu, \quad n = 0, 1, 2 \dots \quad (\text{Equation S6})$$

Using a Boltzmann distribution (Equation S7), where k_B is the Boltzmann constant, these energy differences (ΔE^{CH} , ΔE^{CD}) can be converted into ratios of vibrational energy level populations ($\eta_{v=1}/\eta_{v=0}$) at a given temperature. At 298 K, $\eta_{v=1}^{\text{CH}}/\eta_{v=0}^{\text{CH}} = 0.0049 = 4.9 / 1000$ and $\eta_{v=1}^{\text{CD}}/\eta_{v=0}^{\text{CD}} = 0.0201 = 20.1 / 1000$.

$$\frac{\eta_{v=1}}{\eta_{v=0}} = \exp\left(\frac{-\Delta E}{k_B T}\right) \quad (\text{Equation S7})$$

Next, assume that upon association of the guest to the host exterior, the C–H wagging frequency is reduced by 10 cm^{-1} ; an overall reduction in vibrational frequencies upon guest association must occur, based on the observed EIEs ($K_{d_0}/K_{d_n} > 1$). As with the initial choice of

vibrational frequency, the amount that frequency is reduced upon association is inconsequential, since the overall trend will remain unchanged. Using this reduced C–H wagging frequency, the force constant, C–D vibrational frequency, C–H/D vibrational energy levels and energy level populations are calculated for the guest C–H/D wags in the associated state, as outlined above. At 298 K, the ratio of vibrational populations are $\eta_{v=1}^{CH}/\eta_{v=0}^{CH} = 0.0052 = 5.2 / 1000$ and $\eta_{v=1}^{CD}/\eta_{v=0}^{CD} = 0.0209 = 20.9 / 1000$, for the associated guest C–H/D wagging motions.

Finally, to ascertain how the entropy changes upon guest association for the C–H versus C–D wag, the population differences between the free and associated states are compared. For the C–H wag: there is a population change of +0.2/1000 (increase in entropy) upon guest association, due to the relative changes in the wagging vibrational energy level. For the C–D wag: there is a population change of +0.7/1000 (increase in entropy) upon guest association. Therefore, there is a larger increase in entropy upon guest association to the host exterior for a C–D bond, than for a C–H bond, as a result of changes in wagging vibrational energy level populations. This argument will hold for any C–H/D vibrational motion, so long as the effect of guest association is to lower the vibrational force constant. When the vibrational force constants are lowered upon guest association, the spacing between C–D vibrational energy levels will shrink by more than the spacing between C–H vibrational energy levels, resulting in a wider population distribution and a greater gain in entropy for the deuterated guest.

The above analysis qualitatively predicts exactly what the experimentally determined thermodynamic parameters show: that association of deuterated guests to the host exterior is favored by entropy; or, equivalently, the more favorable association of protiated guests to the host exterior is opposed by entropy. The actual $\Delta\Delta S$ value predicted by this vibrational populations analysis can be calculated from the Boltzmann entropy formula (Equation S8), where p_0 and p_1 are the probabilities of a molecule being in the $v=0$ or $v=1$ vibrational state, respectively. For the isolated C–H/D wag that is reduced by 10 cm^{-1} upon association to the host exterior, the calculated population changes give rise to $\Delta\Delta S = 0.003 \text{ cal mol}^{-1} \text{ K}$. This is roughly two orders of magnitude smaller than the experimentally measured $\Delta\Delta S$ values for the EIEs on exterior association, but the observed EIEs have contributions over all modes of C–H/D vibration and considering only one of these motions will of course give much smaller $\Delta\Delta S$ values. Contributions to the entropic component of the EIE arising from changes in internal bond rotations may also play a role (see reference 14 of the main text). As mentioned in the main text, a detailed and quantitative deconstruction of all possible entropic contributions to the EIE is beyond the scope of the current work. Instead, we believe the qualitative analysis presented above provides a reasonable explanation for the observed experimental trends. In summary, the thermodynamic parameters for EIEs on the binding of guest **2-d_n** to the exterior of host **1** are qualitatively explained by considering only changes in vibrational force constants and ZPEs (enthalpy) and changes in vibrational energy level populations (entropy).

$$S / k_B = p_0 \ln p_0 + p_1 \ln p_1 \quad \text{(Equation S8)}$$

Table S8. DFT-optimized (B3LYP/6-311G++(d,p)) atom coordinates for [2-*d_n*-naphthalene] geometry A (see Figure 7).

| Atom | X | Y | Z | Atom | X | Y | Z |
|------|--------|--------|--------|------|--------|--------|-------|
| C | -0.025 | -3.863 | -2.117 | C | -2.5 | -1.096 | 0.707 |
| C | 1.335 | -3.597 | -2.258 | H | -3.434 | -1.45 | 0.265 |
| C | 1.78 | -2.278 | -2.327 | H | -1.789 | -1.922 | 0.751 |
| C | 0.869 | -1.228 | -2.245 | H | -2.698 | -0.727 | 1.715 |
| C | -0.498 | -1.486 | -2.092 | C | -4.378 | 0.495 | 4.06 |
| C | -0.938 | -2.813 | -2.035 | C | -3.049 | 0.294 | 4.356 |
| H | -0.379 | -4.887 | -2.083 | C | -2.087 | 1.314 | 4.121 |
| H | 2.044 | -4.414 | -2.329 | C | -2.524 | 2.562 | 3.57 |
| H | 2.835 | -2.066 | -2.457 | C | -3.905 | 2.737 | 3.279 |
| H | 1.224 | -0.205 | -2.325 | C | -4.81 | 1.729 | 3.516 |
| H | -1.997 | -3.033 | -1.952 | H | -0.383 | 0.208 | 4.871 |
| C | -1.49 | -0.345 | -2.009 | H | -5.104 | -0.284 | 4.264 |
| H | -2.461 | -0.63 | -2.425 | H | -2.723 | -0.642 | 4.799 |
| H | -1.144 | 0.526 | -2.574 | C | -0.711 | 1.146 | 4.434 |
| P | -1.816 | 0.246 | -0.298 | C | -1.566 | 3.59 | 3.355 |
| C | -3.016 | 1.603 | -0.37 | H | -4.241 | 3.693 | 2.889 |
| H | -3.245 | 1.943 | 0.643 | H | -5.863 | 1.883 | 3.309 |
| H | -2.603 | 2.434 | -0.945 | C | -0.242 | 3.396 | 3.67 |
| H | -3.935 | 1.259 | -0.848 | C | 0.19 | 2.162 | 4.215 |
| C | -0.281 | 0.837 | 0.46 | H | -1.9 | 4.543 | 2.958 |
| H | 0.453 | 0.03 | 0.471 | H | 0.476 | 4.194 | 3.519 |
| H | 0.115 | 1.676 | -0.115 | H | 1.234 | 2.028 | 4.475 |
| H | -0.478 | 1.164 | 1.483 | | | | |

Table S9. DFT-optimized (B3LYP/6-311G++(d,p)) atom coordinates for [2- d_n -7H₂O] geometry B (see Figure 7).

| Atom | X | Y | Z | Atom | X | Y | Z |
|------|--------|--------|--------|------|--------|--------|--------|
| C | -0.076 | -3.788 | -2.346 | H | -3.414 | -1.37 | -0.112 |
| C | 1.298 | -3.575 | -2.43 | H | -1.832 | -1.753 | 0.65 |
| C | 1.798 | -2.274 | -2.437 | H | -2.932 | -0.597 | 1.414 |
| C | 0.926 | -1.19 | -2.355 | O | -3.512 | 2.824 | 2.586 |
| C | -0.455 | -1.394 | -2.263 | H | -3.86 | 3.713 | 2.707 |
| C | -0.947 | -2.704 | -2.264 | H | -4.209 | 2.205 | 2.911 |
| H | -0.472 | -4.796 | -2.357 | O | -0.925 | -0.464 | 4.388 |
| H | 1.976 | -4.418 | -2.503 | H | -0.557 | -0.505 | 5.277 |
| H | 2.865 | -2.101 | -2.519 | H | -0.918 | 0.494 | 4.123 |
| H | 1.325 | -0.181 | -2.382 | O | -1.001 | 2.051 | 3.477 |
| H | -2.017 | -2.881 | -2.221 | H | -0.495 | 2.757 | 3.92 |
| C | -1.402 | -0.217 | -2.186 | H | -1.883 | 2.418 | 3.261 |
| H | -2.364 | -0.454 | -2.65 | O | -5.225 | 0.885 | 3.365 |
| H | -0.997 | 0.65 | -2.717 | H | -4.72 | 0.088 | 3.629 |
| P | -1.785 | 0.361 | -0.48 | H | -5.994 | 0.938 | 3.94 |
| C | -2.931 | 1.761 | -0.618 | O | -3.539 | -1.219 | 3.834 |
| H | -3.16 | 2.144 | 0.381 | H | -3.747 | -2.124 | 4.082 |
| H | -2.474 | 2.554 | -1.213 | H | -2.627 | -1.037 | 4.144 |
| H | -3.854 | 1.438 | -1.102 | O | 0.107 | -1.819 | 2.079 |
| C | -0.272 | 0.898 | 0.348 | H | -0.123 | -1.458 | 2.954 |
| H | 0.36 | 0.029 | 0.533 | H | 0.743 | -2.522 | 2.237 |
| H | 0.246 | 1.629 | -0.276 | O | 0.481 | 4.064 | 4.797 |
| H | -0.524 | 1.354 | 1.31 | H | 1.285 | 4.49 | 4.481 |
| C | -2.57 | -0.973 | 0.455 | H | 0.328 | 4.405 | 5.684 |

Table S10. Vibrational frequencies for the normal modes involving guest methyl group C-H/D motion, calculated for [2- d_n -naphthalene] and [2- d_n -7H₂O] geometries A and B (see Figure 7). Normal modes dominated by methyl group C-H/D motion were selected by Gaussian09 (GaussView) software. The stretching vibrations, whose frequencies are easily distinguished from lower frequency vibrations, are shown in bold.

| Vibrational frequencies (cm ⁻¹) for normal modes of [2- d_n -solvent] isotopologues involving methyl C-H/D motion | | | |
|---|--------------------------------|--------------------------------------|--------------------------------------|
| [2- d_0 -naphthalene] (A) | [2- d_9 -naphthalene] (A) | [2- d_0 -7H ₂ O] (B) | [2- d_9 -7H ₂ O] (B) |
| 171.88 | 122.25 | 192.02 | 138.44 |
| 192.85 | 139.37 | 206.94 | 157.42 |
| 205.66 | 146.58 | 236.49 | 163.67 |
| 210.27 | 224.47 | 837.17 | 237.02 |
| 823.58 | 619.02 | 908.49 | 627.19 |
| 987.65 | 643.20 | 929.51 | 644.00 |
| 991.80 | 650.94 | 998.52 | 659.70 |
| 1005.20 | 686.01 | 1006.04 | 693.87 |
| 1347.85 | 791.69 | 1008.72 | 796.33 |
| 1349.75 | 1043.59 | 1355.51 | 1038.52 |
| 1369.99 | 1045.97 | 1359.96 | 1044.14 |
| 1446.76 | 1046.85 | 1380.72 | 1053.02 |
| 1447.82 | 1050.07 | 1442.68 | 1056.10 |
| 1452.29 | 1052.78 | 1448.85 | 1057.97 |
| 1453.32 | 1054.24 | 1462.35 | 1061.22 |
| 1465.10 | 1056.38 | 1471.57 | 1064.52 |
| 1467.72 | 1059.33 | 1480.39 | 1068.33 |
| 1474.23 | 1063.85 | 1483.48 | 1070.46 |
| 3039.39 | 2180.37 | 3024.99 | 2170.98 |
| 3040.90 | 2181.54 | 3028.13 | 2172.62 |
| 3046.23 | 2184.82 | 3045.37 | 2184.05 |
| 3124.28 | 2315.58 | 3109.47 | 2304.12 |
| 3126.18 | 2316.93 | 3111.63 | 2306.17 |
| 3131.30 | 2320.21 | 3126.99 | 2316.63 |
| 3132.30 | 2321.40 | 3131.44 | 2319.87 |
| 3137.35 | 2325.18 | 3136.44 | 2324.87 |
| 3138.45 | 2326.21 | 3138.89 | 2327.25 |

Table S11. DFT-optimized (B3LYP/6-311G++(d,p)) atom coordinates for [2-*d_n*-naphthalene] geometry C (see Figure 7).

| Atom | X | Y | Z | Atom | X | Y | Z |
|------|--------|--------|---|------|--------|--------|---|
| C | 0.006 | -3.464 | C | C | -2.54 | -0.887 | C |
| C | 1.362 | -3.162 | C | H | -3.48 | -1.225 | H |
| C | 1.777 | -1.831 | C | H | -1.821 | -1.708 | H |
| C | 0.842 | -0.804 | C | H | -2.718 | -0.585 | H |
| C | -0.52 | -1.099 | C | C | 3.899 | -6.613 | C |
| C | -0.93 | -2.437 | C | C | 2.941 | -6.888 | C |
| H | -0.321 | -4.497 | H | C | 1.592 | -7.124 | C |
| H | 2.087 | -3.962 | H | C | 1.242 | -7.071 | C |
| H | 2.828 | -1.591 | H | C | 2.256 | -6.783 | C |
| H | 1.175 | 0.229 | H | C | 3.553 | -6.56 | C |
| H | -1.986 | -2.683 | H | H | 0.848 | -7.473 | H |
| C | -1.538 | 0.015 | C | H | 4.928 | -6.447 | H |
| H | -2.5 | -0.272 | H | H | 3.209 | -6.939 | H |
| H | -1.207 | 0.919 | H | C | 0.579 | -7.42 | C |
| P | -1.884 | 0.517 | P | C | -0.106 | -7.315 | C |
| C | -3.11 | 1.857 | C | H | 1.992 | -6.752 | H |
| H | -3.325 | 2.165 | H | H | 4.32 | -6.353 | H |
| H | -2.724 | 2.714 | H | C | -1.062 | -7.6 | C |
| H | -4.034 | 1.516 | H | C | -0.716 | -7.653 | C |
| C | -0.366 | 1.1 | C | H | -0.368 | -7.286 | H |
| H | 0.386 | 0.31 | H | H | -2.084 | -7.799 | H |
| H | 0.021 | 1.975 | H | H | -1.476 | -7.893 | H |
| H | -0.578 | 1.372 | H | | | | |

Table S12. DFT-optimized (B3LYP/6-311G++(d,p)) atom coordinates for [2- d_n -7H₂O] geometry D (see Figure 7).

| Atom | X | Y | Z | Atom | X | Y | Z |
|------|--------|--------|--------|------|--------|--------|--------|
| C | -0.531 | -3.596 | -1.853 | C | -3.476 | -0.796 | 0.306 |
| C | 0.828 | -3.287 | -1.799 | H | -4.337 | -1.192 | -0.236 |
| C | 1.247 | -1.963 | -1.912 | H | -2.761 | -1.602 | 0.477 |
| C | 0.309 | -0.943 | -2.063 | H | -3.811 | -0.398 | 1.266 |
| C | -1.058 | -1.242 | -2.106 | O | -0.222 | -5.271 | -5.103 |
| C | -1.469 | -2.577 | -2.008 | H | -0.392 | -4.367 | -4.825 |
| H | -0.852 | -4.63 | -1.794 | H | -0.649 | -5.822 | -4.422 |
| H | 1.561 | -4.077 | -1.692 | O | 3.887 | -5.042 | -2.577 |
| H | 2.306 | -1.732 | -1.898 | H | 4 | -4.854 | -1.626 |
| H | 0.646 | 0.083 | -2.174 | H | 4.126 | -4.236 | -3.062 |
| H | -2.523 | -2.829 | -2.078 | O | 4.599 | -2.634 | -4.025 |
| C | -2.081 | -0.138 | -2.262 | H | 5.554 | -2.516 | -4.105 |
| H | -2.965 | -0.48 | -2.809 | H | 4.261 | -2.619 | -4.927 |
| H | -1.673 | 0.718 | -2.81 | O | -0.679 | -6.819 | -2.752 |
| P | -2.689 | 0.521 | -0.658 | H | 0.3 | -6.889 | -2.869 |
| C | -3.903 | 1.836 | -0.967 | H | -1.004 | -7.721 | -2.678 |
| H | -4.27 | 2.236 | -0.02 | O | 6.1 | -2.944 | 1.254 |
| H | -3.44 | 2.643 | -1.538 | H | 6.106 | -2.645 | 2.169 |
| H | -4.746 | 1.438 | -1.535 | H | 7.023 | -3.055 | 1.007 |
| C | -1.308 | 1.202 | 0.298 | O | 4.03 | -4.6 | 0.199 |
| H | -0.558 | 0.425 | 0.457 | H | 4.729 | -4.013 | 0.537 |
| H | -0.853 | 2.032 | -0.244 | H | 4.136 | -5.419 | 0.69 |
| H | -1.67 | 1.561 | 1.264 | O | 1.873 | -6.664 | -3.588 |

Table S13. Vibrational frequencies for the normal modes involving guest aromatic C-H/D motion, calculated for [2- d_n -naphthalene] and [2- d_n -7H₂O] geometries C and D (see Figure 7). Normal modes dominated by guest aryl C-H/D motion were selected by Gaussian09 (GaussView) software. The stretching vibrations, whose frequencies are easily distinguished from lower frequency vibrations, are shown in bold.

| Vibrational frequencies (cm ⁻¹) for normal modes of [2- d_n -solvent] isotopologues involving aryl C-H/D motion | | | |
|---|--------------------------------|--------------------------------------|--------------------------------------|
| [2- d_0 -naphthalene] (C) | [2- d_5 -naphthalene] (C) | [2- d_0 -7H ₂ O] (D) | [2- d_5 -7H ₂ O] (D) |
| 858.98 | 360.92 | 789.43 | 363.82 |
| 942.19 | 546.96 | 866.12 | 548.93 |
| 997.93 | 560.62 | 944.07 | 560.25 |
| 1028.12 | 668.44 | 1006.86 | 675.59 |
| 1103.27 | 811.64 | 1045.36 | 818.17 |
| 1193.94 | 842.10 | 1103.89 | 843.72 |
| 1206.73 | 857.56 | 1201.57 | 856.45 |
| 1362.41 | 865.34 | 1217.17 | 873.18 |
| 1487.03 | 886.28 | 1364.38 | 892.06 |
| 1525.26 | 1055.24 | 1527.59 | 1057.88 |
| 3155.57 | 2330.38 | 3152.23 | 2328.01 |
| 3156.22 | 2331.06 | 3153.28 | 2328.94 |
| 3183.82 | 2352.58 | 3182.64 | 2355.42 |
| 3191.94 | 2361.95 | 3188.70 | 2359.10 |
| 3202.34 | 2374.38 | 3211.91 | 2379.41 |

Details of M06-2X calculations

Calculations using the M06-2X functional, which has been shown to more accurately calculate energies in some cases where noncovalent interactions are important (J. Comput. Chem. **2009**, *30*, 51), were carried out in order to verify that our original B3LYP-based calculations reported in the manuscript were not overly simplistic and did not fail to account for significant dispersion interactions. Starting from the B3LYP-minimized geometries, structures A and B were minimized with M06-2X/6-311G++(d,p). The geometries did change from those generated by the B3LYP calculations (Figure S46); most notably, the naphthalene ring in structure A moves ~ 0.5 Å closer to the phosphonium group. The calculated ZPEs for each geometry also change significantly (Table S14), but despite the geometry and ZPE changes, the overall EIE calculated from those M06-2X-determined ZPEs is $Kd_0/Kd_9 = 1.30$, slightly larger, but very much consistent, with the B3LYP-determined EIE of $Kd_0/Kd_9 = 1.16$. Furthermore, closer analysis of the changes in methyl/benzyl C-H vibrational frequencies reveals that, as observed for the B3LYP calculations, the EIE is dominated by lower frequency vibrational motions, while C-H stretching frequencies play a negligible role (for the M06-2X calculations: $\Delta\Delta\Sigma\nu(\text{stretch}) = 1.19$ cm^{-1} and $\Delta\Delta\Sigma\nu(\text{low}) = 1552$ cm^{-1}). Similar calculations were carried out on structures C and D, but after many iterations of adjusting geometry and convergence criteria, geometry D failed to successfully converge at the M06-2X/6-311G++(d,p) level of theory, so the C vs D comparison is not made with this functional. However, the calculations comparing A and B with the M06-2X functional, which show good agreement with the original B3LYP calculations, are sufficient to show that the explicit correction for dispersion interactions in M06-2X does not significantly affect the calculated EIE, or our interpretation of the origin of that effect (it is not unlikely that because the EIEs are differences of differences of ZPEs, much of the importance in accurately calculating the absolute magnitude of dispersion interactions is washed out).

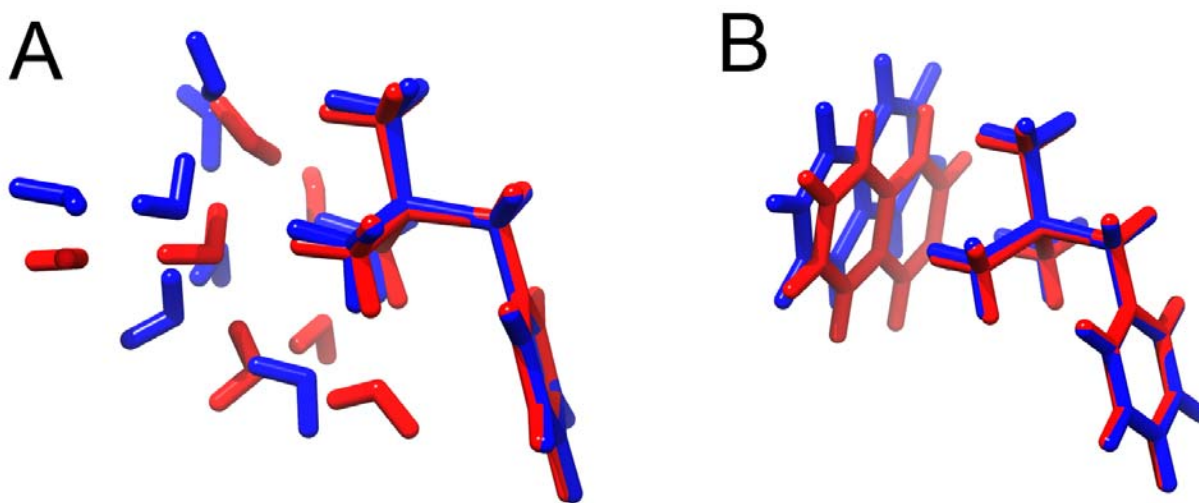


Figure S46. Overlay of M06-2X/6-311G++(d,p)-calculated geometry (red) and B3LYP/6-311G++(d,p)-calculated geometry (blue), for model guest-solvent complexes A and B. Although the minimized geometries differ for the M06-2X versus B3LYP calculations, the EIEs calculated from ZPE changes (Table S14) are very similar. Structural alignments and images generated using UCSF Chimera.¹

Table S14. Calculated ZPEs for isotopologues of [**2-d_n**-solvent] geometries A and B using M06-2X/6-311G++(d,p).

| Geometry | Isotopologue | ZPE (kcal/mol) | Δ ZPE ^a (kcal/mol) | $\Delta\Delta$ ZPE ^b (kcal/mol) |
|----------|--|-------------------|---|---|
| A | [2-d₀ -naphthalene] | 258.54 | 18.115 | 0.17 |
| | [2-d₉ -naphthalene] | 240.43 | | |
| B | [2-d₀ -7H ₂ O] | 241.18 | 17.945 | |
| | [2-d₉ -7H ₂ O] | 223.24 | | |

^a Δ ZPE = ZPE(**2-d₀**-X) – ZPE(**2-d_n**-X); where X = naphthalene or 7H₂O and n = 5 or 9.

^b $\Delta\Delta$ ZPE = Δ ZPE(**2-d_n**-7H₂O) – Δ ZPE(**2-d_n**-naphthalene).

Although both the geometries and ZPEs are different in the M06-2X versus B3LYP calculations, the EIEs, which are calculated from the relative spacing of ZPEs (i.e. $\Delta\Delta$ ZPE), are quite similar ($K_{d_0}/K_{d_9} = 1.30$ for M06-2X and 1.16 for B3LYP) and both are very much consistent with the experimentally observed EIE for **2-d₀** versus **2-d₉** ($K_{d_0}/K_{d_9} = 1.14(1)$). Furthermore, contributions to the EIE from methyl/benzyl C-H vibrational modes are qualitatively consistent between the M06-2X and B3LYP calculations: with B3LYP $\Delta\Delta\Sigma\nu(\text{stretch}) = -17.15 \text{ cm}^{-1}$ and $\Delta\Delta\Sigma\nu(\text{low}) = 210.36 \text{ cm}^{-1}$, and for M06-2X $\Delta\Delta\Sigma\nu(\text{stretch}) = 1.19 \text{ cm}^{-1}$ and $\Delta\Delta\Sigma\nu(\text{low}) = 1552 \text{ cm}^{-1}$. In both cases, the low frequency methyl/benzyl C-H vibrational modes dominate the observed EIE and the stretching vibrational modes either oppose the EIE or are negligible in magnitude.

Full citation for reference 47 in manuscript:

- (47) Frisch, M. J.; Trucks, G. W.; Schlegel, H. B.; Scuseria, G. E.; Robb, M. A.; Cheeseman, J. R.; Scalmani, G.; Barone, V.; Mennucci, B.; Petersson, G. A.; Nakatsuji, H.; Caricato, M.; Li, X.; Hratchian, H. P.; Izmaylov, A. F.; Bloino, J.; Zheng, G.; Sonnenberg, J. L.; Hada, M.; Ehara, M.; Toyota, K.; Fukuda, R.; Hasegawa, J.; Ishida, M.; Nakajima, T.; Honda, Y.; Kitao, O.; Nakai, H.; Vreven, T.; Montgomery, Jr., J. A.; Peralta, J. E.; Ogliaro, F.; Bearpark, M.; Heyd, J. J.; Brothers, E.; Kudin, K. N.; Staroverov, V. N.; Kobayashi, R.; Normand, J.; Raghavachari, K.; Rendell, A.; Burant, J. C.; Iyengar, S. S.; Tomasi, J.; Cossi, M.; Rega, N.; Millam, N. J.; Klene, M.; Knox, J. E.; Cross, J. B.; Bakken, V.; Adamo, C.; Jaramillo, J.; Gomperts, R.; Stratmann, R. E.; Yazyev, O.; Austin, A. J.; Cammi, R.; Pomelli, C.; Ochterski, J. W.; Martin, R. L.; Morokuma, K.; Zakrzewski, V. G.; Voth, G. A.; Salvador, P.; Dannenberg, J. J.; Dapprich, S.; Daniels, A. D.; Farkas, Ö.; Foresman, J. B.; Ortiz, J. V.; Cioslowski, J.; Fox, D. J. *Gaussian 09*, Revision A.02, Gaussian, Inc.: Wallingford CT, 2009.

References for Supporting Information

- (1) UCSF Chimera--a visualization system for exploratory research and analysis. Pettersen EF, Goddard TD, Huang CC, Couch GS, Greenblatt DM, Meng EC, Ferrin TE. *J Comput Chem.* 2004 Oct;25(13):1605-12.